

General relativistic self-gravitating equilibrium disks around rotating neutron stars

Yoonsoo Kim^{1,2*}, Jinho Kim³, Hee Il Kim⁴, and Hyung Mok Lee⁵

¹ *Theoretical Astrophysics, Mailcode 350-17, California Institute of Technology, Pasadena, CA 91125, USA*

² *Department of Physics & Astronomy, Seoul National University, 1 Gwanak-ro, Gwanak-gu, Seoul 08826, South Korea*

³ *Korea Astronomy and Space Science Institute, 776 Daedeok-daero, Yuseong-gu, Daejeon 34055, South Korea*

⁴ *Center for Quantum Spacetime, Sogang University, 35 Baekbeom-ro, Mapo-gu, Seoul 04107, South Korea*

⁵ *Center for the Gravitational-Wave Universe, Astronomy Research Center, Seoul National University, 1 Gwanak-ro, Gwanak-gu, Seoul 08826, South Korea*

Accepted XXX. Received YYY; in original form ZZZ

ABSTRACT

In modeling a relativistic disk around a compact object, the self-gravity of the disk is often neglected while it needs to be incorporated for more accurate descriptions in several circumstances. Extending the Komatsu-Eriguchi-Hachisu self-consistent field method, we present numerical models of a rapidly rotating neutron star with a self-gravitating disk in stationary equilibrium. In particular, our approach allows us to obtain numerical solutions involving a massive disk with the rest mass $O(10^{-1}) - O(10^0) M_{\odot}$ closely attached to a rotating neutron star, given that the disk is mainly supported by the relativistic electron degeneracy pressure. We also assess the impact of self-gravity on the internal structure of the disk and the neutron star. These axisymmetric, stationary solutions can be employed for simulations involving the neutron star-disk system in the context of high-energy transients and gravitational wave emissions.

Key words: hydrodynamics – methods: numerical – stars: neutron

1 INTRODUCTION

Along with recent breakthroughs in multi-messenger astronomy (Abbott et al. 2016, 2017; Kasliwal et al. 2017), theoretical studies on compact objects and the dynamics of relativistic matter surrounding them have a growing significance. General relativistic approaches are required to properly describe astrophysical phenomena taking place in a strong gravity regime, yet the high complexity and nonlinearity of the Einstein field equations compel numerical approaches to obtain solutions (Baumgarte & Shapiro 2010; Rezzolla & Zanotti 2013). Particularly simple as well as useful are the equilibrium models of relativistic stars with disks, which serve as not only a means to study long-term secular evolutions of such systems but also as initial data of time-dependent numerical relativity simulations.

Numerical schemes for studying the structure of rotating neutron stars have been developed in a variety of flavors (see e.g. Paschalidis & Stergioulas (2017) for a review on this topic). Of particular interest is the work by Hachisu (1986), who proposed a novel iterative self-consistent field method to construct equilibrium models of rotating stars in the Newtonian framework. Based on a similar strategy, Komatsu, Eriguchi & Hachisu (1989a) constructed equilibrium models of uniformly rotating neutron stars in full general relativity, and subsequently extended to differential rotation (Komatsu et al. 1989b). This so-called the KEH method, which is named after the three authors of the original work, has been widely employed for studying rotating neutron stars (e.g. Cook et al. 1992, 1994a,b; Eriguchi et al. 1994; Stergioulas & Friedman 1995; Nozawa et al. 1998; Bauswein

& Stergioulas 2017; Iosif & Stergioulas 2021, 2022) along with some modifications made in later studies.

With the aim of modeling accretion disks around a black hole, the theory of an equilibrium disk (torus) had been developed more in the context of a non-self-gravitating fluid in a fixed background spacetime (e.g. Fishbone & Moncrief 1976; Kozłowski et al. 1978; Abramowicz et al. 1978) in its early stage. In particular, disk solutions by Fishbone & Moncrief (1976) have been extensively used to initialize the matter distribution in black hole accretion simulations. In most simulations of accreting compact objects, the self-gravity of the disk can be often ignored to simplify the problem, owing to its small mass compared to the central object (Abramowicz & Fragile 2013). However, this assumption might no longer be valid in some astrophysical scenarios such as an accreting nascent compact object in core-collapse supernovae (e.g. Fryer 1999; Chan et al. 2018; Burrows et al. 2023) or a massive remnant disk formed after disruption of a neutron star during compact binary merger events (e.g. Foucart 2012; Foucart et al. 2016; Radice et al. 2018; Bernuzzi 2020; Krüger & Foucart 2020; Camilletti et al. 2024).

While early works on the relativistic, self-gravitating disks have mainly explored black hole disks (Will 1974; Chakrabarti 1988; Lanza 1992; Nishida & Eriguchi 1994; Ansorg & Petroff 2005; Shibata 2007), it has been suggested that a massive disk can be formed around a neutron star from the accretion-induced collapse of a white dwarf (Abdikamalov et al. 2010) or binary neutron star mergers with asymmetric mass ratios ($q \sim 0.75 - 0.85$, Rezzolla et al. 2010).

Equilibrium solutions of the neutron star-disk system can be used as initial data for a range of astrophysical scenarios that can emerge from such a system. Possible applications include investigating con-

* ykim7@caltech.edu

Table 1. Units of some physical quantities when $c = G = M_\odot = 1$.

Quantity	Conversion factor	Unit physical scale in cgs
Length	GM_\odot/c^2	$1.477 \times 10^5 \text{cm}$
Time	GM_\odot/c^3	$4.927 \times 10^{-6} \text{s}$
Frequency	$c^3/(GM_\odot)$	$2.030 \times 10^5 \text{Hz}$
Mass	M_\odot	$1.988 \times 10^{33} \text{g}$
Mass Density	$c^6/(G^3 M_\odot^2)$	$6.173 \times 10^{17} \text{g cm}^{-3}$

nections between X-ray quasi-periodic oscillations and disk oscillation modes (e.g. [Blaes et al. 2006](#); [Fragile et al. 2018](#); [Matuszková et al. 2024](#)), hydrodynamic instabilities of the self-gravitating disk (see [Wessel et al. 2021](#), for the black hole-disk system), the collapse of the disk via neutron star burst-disk interaction ([Fragile et al. 2018](#)), disk-fed jet launching from a neutron star ([Das & Porth 2024](#)), and accretion-induced collapse of the system into a black hole ([Giacomazzo & Perna 2012](#)). Some of the aforementioned scenarios are expected to launch electromagnetic signals such as gamma-ray bursts or emit gravitational waves that can be observed with next-generation detectors.

Fully general relativistic models of a neutron star with a self-gravitating disk, to the best of our knowledge, were first studied by [Nishida et al. \(1992\)](#). Based on the KEH scheme, they presented a set of numerical equilibrium solutions of a uniformly rotating neutron star and a torus subject to the differential rotation law suggested by [Komatsu et al. \(1989b\)](#). Albeit the self-gravity was neglected, we also mention the work of [Corvino \(2009\)](#), TORERO code) which constructed equilibrium disk around a rotating neutron star and was used to prepare initial data of accretion-induced collapse simulations in [Giacomazzo & Perna \(2012\)](#).

In this paper, we present equilibrium models of a rapidly rotating neutron star with a self-gravitating disk based on the KEH scheme with an extension made to construct a disk. Our formulation, specifically compared to the work of [Nishida et al. \(1992\)](#), uses the specific angular momentum as a basic variable describing the rotation of the disk, providing a more direct and flexible control over the angular momentum distribution of the disk. We also attempt to quantitatively analyze the impact of the self-gravity of the disk on the neutron star-disk equilibrium solutions.

This article is organized as follows. In Sec. 2, we review basic equations describing general relativistic rotating fluid bodies in stationary equilibrium. We introduce our iterative numerical scheme and its implementation in Sec. 3. Computed equilibrium models and discussions on the disk self-gravity are presented in Sec. 4, and we conclude with a summary in Sec. 5. Throughout this paper we adopt $c = G = M_\odot = 1$ unit; conversion rules for some physical quantities are given in Table 1. We use the abstract index notation with Latin indices (a, b, \dots) for spacetime tensors.

2 ROTATING FLUID BODIES IN GENERAL RELATIVITY

2.1 Basic equations

We consider a stationary and axisymmetric configuration of spacetime geometry and matter distribution. The spacetime metric can be written as

$$\begin{aligned}
 ds^2 &= g_{tt} dt^2 + g_{rr} dr^2 + g_{\theta\theta} d\theta^2 + 2g_{t\phi} dt d\phi + g_{\phi\phi} d\phi^2 \\
 &= -e^{\gamma+\varrho} dt^2 + e^{2\alpha} (dr^2 + r^2 d\theta^2) + e^{\gamma-\varrho} r^2 \sin^2 \theta (d\phi - \omega dt)^2,
 \end{aligned} \tag{1}$$

where metric functions $\varrho, \gamma, \alpha, \omega$ depend on r and θ coordinates only. We model matter as the perfect fluid, which has the stress-energy tensor

$$T^{ab} = (\rho_0 + \rho_i + p)u^a u^b + p g^{ab}, \tag{2}$$

where ρ_0 is rest energy density, ρ_i is internal energy density, and p is pressure measured in the rest frame of the fluid. u^a is the fluid 4-velocity. We assume the fluid follows a barotropic equation of state $p = p(\rho_0)$. In this work, we only consider the polytropic law for the equation of state, expressed as

$$p = K \rho_0^\Gamma \tag{3}$$

where K is the polytropic constant and Γ is the polytropic exponent. It follows from the first law of thermodynamics that

$$\rho_i = \frac{p}{\Gamma - 1}. \tag{4}$$

It is further assumed that the fluid is purely circularly rotating without any meridional motion; the fluid 4-velocity has a form

$$u^a = (u^t, 0, 0, u^\phi) = u^t (1, 0, 0, \Omega), \tag{5}$$

where $\Omega = u^\phi/u^t = d\phi/dt$ is the coordinate angular velocity. From the normalization condition of the fluid 4-velocity ($u^a u_a = -1$), we get

$$u^t = \left[- (g_{tt} + 2g_{t\phi}\Omega + g_{\phi\phi}\Omega^2) \right]^{-1/2} = \frac{e^{-(\gamma+\varrho)/2}}{\sqrt{1-V^2}}, \tag{6}$$

where $V = e^{-\varrho} (\Omega - \omega) r \sin \theta$.

From Eqs. (1) and (2), it is straightforward to evaluate the curvature tensor and write out the field equations for each component. Following [Komatsu et al. \(1989a\)](#), we use the following form:

$$\nabla^2 (\varrho e^{\gamma/2}) = S_\varrho (g_{ab}, T_{ab}) \tag{7}$$

$$\left[\nabla^2 + \frac{1}{r} \frac{\partial}{\partial r} - \frac{1}{r^2} \mu \frac{\partial}{\partial \mu} \right] (\gamma e^{\gamma/2}) = S_\gamma (g_{ab}, T_{ab}) \tag{8}$$

$$\left[\nabla^2 + \frac{2}{r} \frac{\partial}{\partial r} - \frac{2}{r^2} \mu \frac{\partial}{\partial \mu} \right] (\omega e^{(\gamma-2\varrho)/2}) = S_\omega (g_{ab}, T_{ab}) \tag{9}$$

$$\frac{\partial \alpha}{\partial \mu} = S_\alpha (g_{ab}, T_{ab}) \tag{10}$$

where $\mu = \cos \theta$ and ∇^2 is the Laplacian operator in the flat space. The detailed form of the source terms $S_\varrho, S_\gamma, S_\omega, S_\alpha$ in Eq. (7)-(10) can be looked up from several references which include technical descriptions of the KEH scheme (e.g. [Komatsu et al. 1989a](#); [Cook et al. 1992](#); [Rezzolla & Zanotti 2013](#)).

The equation of motion $\nabla_a T^{ab} = 0$ gives the relativistic Euler equation

$$-\partial_a \ln u^t + j(\Omega) \partial_a \Omega = -\frac{\partial_a p}{\rho_0 + \rho_i + p}, \tag{11}$$

where

$$j(\Omega) \equiv u^t u_\phi = \frac{l}{1 - \Omega l} \tag{12}$$

and

$$l \equiv -\frac{u_\phi}{u_t} = -\frac{g_{t\phi} + \Omega g_{\phi\phi}}{g_{tt} + \Omega g_{t\phi}} \tag{13}$$

is the specific angular momentum.

The relativistic von Zeipel's theorem ([Abramowicz 1971](#)) states that the Euler equation (11) is integrable if equi-pressure and equi-energy density surfaces coincide i.e., if the equation of state is

barotropic. Since the adopted polytropic equation of state (3) satisfies the criterion, Eq. (11) can be integrated into

$$-\ln u^t + \int j(\Omega) d\Omega + \ln H = C, \quad (14)$$

where C is an integral constant and

$$\ln H \equiv \int \frac{dp}{\rho_0 + \rho_i + p} = \ln \left[1 + \frac{\Gamma}{\Gamma - 1} K \rho_0^{\Gamma - 1} \right]. \quad (15)$$

The relativistic Euler equation in its integral form Eq. (14) describes the matter distribution within a single rotating fluid body, where the integration constant C can be determined by imposing proper boundary conditions. Depending on how the boundary conditions are imposed, the fluid body (the region with $\ln H > 0$) can be in either a spheroidal (star) or toroidal (disk or torus) configuration.

2.2 Equilibrium solutions

Specifying the functional form of $j(\Omega)$ amounts to choosing a specific rotation profile of a fluid body. For rotating neutron star models, one of the most widely used one is the one-parameter law $j(\Omega) = A^2(\Omega_c - \Omega)$ (Komatsu et al. 1989a), where A is a free parameter that controls the degree of differential rotation and Ω_c is angular velocity on the rotation axis. In this work, we only consider the uniformly rotating neutron star, for which Eq. (14) simplifies to $\ln(H/u^t) = C$.

While the theory of a relativistic rotating star and an equilibrium torus have all theoretical grounds in common apart from their topology (spheroidal or toroidal), it is useful, when describing an equilibrium torus, to rewrite the governing equations by changing the primary variable of rotation from angular velocity Ω to the specific angular momentum l (e.g. Kozłowski et al. 1978; Abramowicz et al. 1978; Font & Daigne 2002). Using the following relation

$$\Omega = -\frac{g_{t\phi} + g_{tt}l}{g_{\phi\phi} + g_{t\phi}l}, \quad (17)$$

the relativistic Euler equation (11) can be rewritten to an equivalent form

$$\partial_\alpha \ln |u_t| + u_t u^\phi \partial_\alpha l = -\frac{\partial_\alpha p}{\rho_0 + \rho_i + p}, \quad (18)$$

which can then be integrated to give

$$\ln |u_t| + \int u_t u^\phi dl + \ln H = C, \quad (19)$$

where

$$|u_t|^2 = \frac{g_{t\phi}^2 - g_{tt}g_{\phi\phi}}{g_{tt}l^2 + 2g_{t\phi}l + g_{\phi\phi}} \quad (20)$$

and

$$u_t u^\phi = -\frac{\Omega}{1 - \Omega l} = \frac{g_{t\phi} + g_{tt}l}{g_{tt}l^2 + 2g_{t\phi}l + g_{\phi\phi}}. \quad (21)$$

For a given background metric $g_{\mu\nu}$, three characteristic values of specific angular momentum l_{cr} , l_b , l_K can be defined as follows. First, positivity of the denominator in Eq. (20) imposes the following constraint on the specific angular momentum l :

$$l_{\text{cr}}^-(r, \theta) < l(r, \theta) < l_{\text{cr}}^+(r, \theta) \quad (22)$$

where

$$l_{\text{cr}}^\pm = \frac{g_{t\phi} \pm \sqrt{g_{t\phi}^2 - g_{tt}g_{\phi\phi}}}{-g_{tt}}. \quad (23)$$

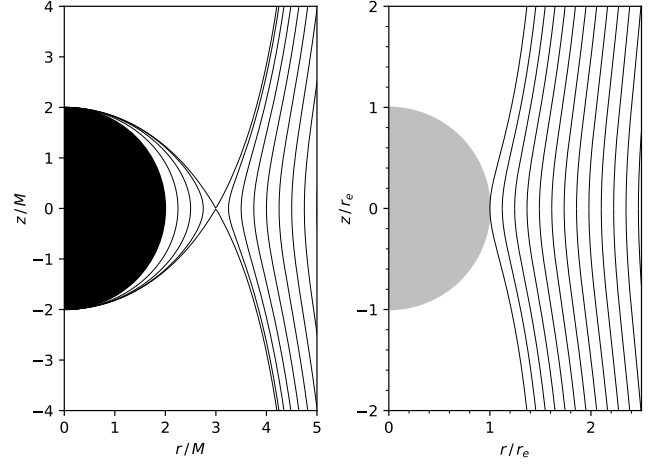


Figure 1. The von Zeipel's cylinders (see Sec. 2.2.1) of a Schwarzschild black hole (left panel) and of a $M_0 = 1.8M_\odot$ spherical neutron star with the $K = 100$, $\Gamma = 2$ polytropic equation of state (right panel).

Matter is gravitationally bound to the system if $-u_t < 1$, which sets the following condition

$$l_b^-(r, \theta) < l < l_b^+(r, \theta) \quad (24)$$

where

$$l_b^\pm = \frac{g_{t\phi} \pm \sqrt{(g_{t\phi}^2 - g_{tt}g_{\phi\phi})(1 + g_{tt})}}{-g_{tt}}. \quad (25)$$

Finally, on the equatorial plane, the Keplerian angular momentum is given as

$$l_K^\pm = \frac{-B \pm \sqrt{B^2 - AC}}{A} \quad (26)$$

where the coefficients A , B , and C are given by

$$\begin{aligned} A &= -g_{t\phi}^2 \frac{\partial g_{tt}}{\partial r} + 2g_{tt}g_{t\phi} \frac{\partial g_{t\phi}}{\partial r} - g_{tt}^2 \frac{\partial g_{\phi\phi}}{\partial r}, \\ B &= -g_{t\phi}g_{\phi\phi} \frac{\partial g_{tt}}{\partial r} + (g_{t\phi}^2 + g_{tt}g_{\phi\phi}) \frac{\partial g_{t\phi}}{\partial r} - g_{tt}g_{t\phi} \frac{\partial g_{\phi\phi}}{\partial r}, \\ C &= -g_{\phi\phi}^2 \frac{\partial g_{tt}}{\partial r} + 2g_{t\phi}g_{\phi\phi} \frac{\partial g_{t\phi}}{\partial r} - g_{tt}^2 \frac{\partial g_{\phi\phi}}{\partial r}. \end{aligned} \quad (27)$$

If the matter is rotating with l_K^\pm on the equatorial plane, the motion is purely geodesic and the right hand side of Eq. (18) vanishes (i.e. pressure gradient is zero).

2.2.1 Von Zeipel's cylinders

A further consequence of the relativistic von Zeipel's theorem (Abramowicz 1971) is that when the Euler equation (11) is integrable, const- Ω surfaces coincide with const- l surfaces i.e. $\Omega = \Omega(l)$. These surfaces are called the von Zeipel cylinders¹. For a specific value of l_0 and the corresponding value of Ω_0 related by Eq. (17), the equation

$$g_{tt}(r, \theta)l_0 + (1 + \Omega_0 l_0)g_{t\phi}(r, \theta) + g_{\phi\phi}(r, \theta)\Omega_0 = 0 \quad (28)$$

¹ While these surfaces are cylinders in the Newtonian regime, cylindrical topology is only asymptotic in general relativistic cases (Abramowicz 1974, see also Figure 1).

describes a single von Zeipel's cylinder characterized by l_0 (or equivalently, by Ω_0) in terms of the coordinates (r, θ) .

When the specific angular momentum profile on the equatorial plane $l_{\text{eq}}(r)$ is specified, Eq. (17) gives the corresponding profile of the angular velocity on the equatorial plane:

$$\Omega_{\text{eq}}(r) = \Omega(r, \pi/2) = -\frac{g_{t\phi}(r, \pi/2) + g_{tt}(r, \pi/2)l_{\text{eq}}(r)}{g_{\phi\phi}(r, \pi/2) + g_{t\phi}(r, \pi/2)l_{\text{eq}}(r)}. \quad (29)$$

Combining Eq. (28) and (29), a von Zeipel's cylinder intersecting the equatorial plane at the radius r_0 is described by an equation

$$l_{\text{eq}}^2(r_0)[g_{t\phi}(r_0, \pi/2)g_{tt}(r, \theta) - g_{tt}(r_0, \pi/2)g_{t\phi}(r, \theta)] \\ + l_{\text{eq}}(r_0)[g_{\phi\phi}(r_0, \pi/2)g_{tt}(r, \theta) - g_{tt}(r_0, \pi/2)g_{\phi\phi}(r, \theta)] \\ + [g_{\phi\phi}(r_0, \pi/2)g_{t\phi}(r, \theta) - g_{t\phi}(r_0, \pi/2)g_{\phi\phi}(r, \theta)] = 0. \quad (30)$$

For example, in the Schwarzschild spacetime, Eq. (30) simplifies to

$$(r_0 - 2M)r^3 \sin^2 \theta - r_0^3(r - 2M) = 0. \quad (31)$$

See e.g. [Daigne & Font \(2004\)](#) for the structure of von Zeipel's cylinders in the Kerr spacetime for different values of the black hole spin. When an analytic expression of the spacetime metric is not available, Eq. (30) needs to be numerically solved to obtain the structure of the von Zeipel's cylinders.

In Figure 1, we show the von Zeipel's cylinders outside the horizon of a Schwarzschild black hole and the surface of a spherical neutron star with the rest mass $M_0 = 1.8M_\odot$ and $K = 100$, $\Gamma = 2$ polytropic equation of state. Note that the cusp at $r = 3M$ for the black hole (left panel of Figure 1) does not appear for the neutron star (right panel).

2.2.2 Equipotential surfaces and matter distribution

The relativistic Euler equation in an alternative form (19) can be rearranged as

$$W = C - \ln H, \quad (32)$$

where the effective potential W is defined as

$$W = \ln |u_t| - \int \frac{\Omega dl}{1 - \Omega l}. \quad (33)$$

Applying Eq. (33) between two points $(r, \pi/2)$ and $(\infty, \pi/2)$ on the equatorial plane,

$$W_{\text{eq}}(r) = W(r, \pi/2) \\ = \ln |u_t(r, \pi/2)| - \int_{\infty}^r \frac{\Omega_{\text{eq}}}{1 - \Omega_{\text{eq}}l_{\text{eq}}} \frac{dl_{\text{eq}}(r)}{dr} dr \quad (34)$$

where we use a fiducial offset $W = 0$ at the infinity. If there is a von Zeipel's cylinder passing through two points (r, θ) and $(r_0, \pi/2)$, since it is a constant- l surface, using Eq. (33) and (34) we get

$$W(r, \theta) = W_{\text{eq}}(r_0) + \ln \frac{u_t(r, \theta)}{u_t(r_0, \pi/2)} \\ = \ln |u_t(r, \theta)| - \int_{\infty}^{r_0} \frac{\Omega_{\text{eq}}}{1 - \Omega_{\text{eq}}l_{\text{eq}}} \frac{dl_{\text{eq}}(r)}{dr} dr. \quad (35)$$

Note that the variable r_0 in the equation (34) is a function of (r, θ) , which depends on the detailed geometry of the von Zeipel's cylinders in a given spacetime. Plugging in Eq. (20) and (21), we have

$$W(r, \theta) = \frac{1}{2} \ln \frac{g_{t\phi}^2 - g_{tt}g_{\phi\phi}}{g_{tt}l^2 + 2g_{t\phi}l + g_{\phi\phi}} \\ + \int_{\infty}^{r_0(r, \theta)} \frac{g_{t\phi} + g_{tt}l_{\text{eq}}}{g_{tt}l_{\text{eq}}^2 + 2g_{t\phi}l_{\text{eq}} + g_{\phi\phi}} \frac{dl_{\text{eq}}(r)}{dr} dr \quad (36)$$

Table 2. List of parameters specifying a single equilibrium model.

Parameters	Description
ρ_0^{max}	Neutron star maximum rest mass density
r_p/r_e	Neutron star axis ratio
κ, a	Angular momentum distribution of the disk on the equatorial plane
W_{in} (or r_{in})	Inner edge of the disk

Given a spacetime metric and an angular momentum profile $l_{\text{eq}}(r)$ on the equatorial plane, one can obtain the matter distribution of an equilibrium disk through the following procedure. 1) Solve the equation (30) at each points to find $r_0(r, \theta)$, which is the coordinate radius of the point at which the von Zeipel's cylinder passing through a point (r, θ) intersects the equatorial plane. 2) Determine $l(r, \theta) = l_{\text{eq}}(r_0)$, so one can compute $W(r, \theta)$ with Eq. (36). 3) Choose the radius of the inner edge of the disk $r = r_{\text{in}}$ on the equatorial plane to determine $W_{\text{in}} = W(r_{\text{in}}, \pi/2)$, which amounts to imposing the boundary condition of the Euler equation (19). 4) Compute the specific enthalpy at every point using

$$\ln H(r, \theta) = W_{\text{in}} - W(r, \theta) \quad (37)$$

to recover the rest energy density from Eq. (15).

In this work, we assume that the distribution of the specific angular momentum on the equatorial plane follows the power law (e.g. [Daigne & Font 2004](#))

$$l_{\text{eq}}(r) \equiv l(r, \pi/2) = \kappa \left(\frac{r}{r_e} \right)^a \quad (38)$$

within the disk, where κ is a constant, $a \geq 0$ is a power index, and r_e is the coordinate radius of the neutron star.

3 NUMERICAL IMPLEMENTATION

3.1 Computational procedure

In this section, we describe our iterative method for constructing a numerical equilibrium model of a neutron star with a self-gravitating disk. Hereafter subscripts "NS" and "Disk" are used to denote quantities related to the neutron star and the equilibrium disk, respectively.

First, a numerical model of an isolated rotating neutron star is constructed following the KEH scheme (e.g. [Komatsu et al. 1989a; Cook et al. 1992](#)). This requires two parameters fixed: the maximum rest energy density ρ_0^{max} and the neutron star axis ratio r_p/r_e . Once we converge to a rotating neutron star model with the desired values of $(\rho_0^{\text{max}}, r_p/r_e)$ in the computational space, we choose the rotation parameters (κ, a) to fix the specific angular momentum distribution $l_{\text{eq}}(r)$ of the disk on the equatorial plane (see Sec. 3.2 for the details). Keeping all the parameters $(\rho_0^{\text{max}}, r_p/r_e, \kappa, a)$ fixed, each iteration step proceeds as follows:

- (i) Make an initial guess on spacetime metric and matter distribution, which we denote by $g^{(n)}$ and $T^{(n)}$, where n is the iteration number.
- (ii) Evaluate the source terms in field equations (7) - (10) using $g^{(n)}$ and $T^{(n)}$, then integrate the field equations to compute updated metric $g^{(n+1)}$.
- (iii) *Building a neutron star* : Apply hydrodynamic boundary conditions for the neutron star by applying Eq. (16) simultaneously at the pole, the equator, and the center of the neutron star. The coordinate radius $r_e^{(n+1)}$ and the angular velocity $\Omega_0^{(n+1)}$ of the neutron star are determined in this step. Then compute

In $H_{\text{NS}}(r, \theta)$ with the equation (16) to obtain an updated matter distribution $T_{\text{NS}}^{(n+1)}$ of the neutron star.

- (iv) *Building a disk*: Follow the procedure outlined in Sec. 2.2.2 to construct an equilibrium disk. At the grid points outside the surface of the neutron star, solve Eq. (30) to get the values of $r_0(r, \theta)^2$ and compute the effective potential $W(r, \theta)$ using Eq. (36). Pick a value of W_{in} , (or equivalently, pick the inner edge radius r_{in} of the disk at which $W_{\text{in}} \equiv W_{\text{eq}}(r_{\text{in}})$), then compute $\ln H_{\text{Disk}}$ with Eq. (37) to get the updated matter distribution $T_{\text{Disk}}^{(n+1)}$ of the disk.
- (v) Feed $g^{(n+1)}$ and $T^{(n+1)} = T_{\text{NS}}^{(n+1)} + T_{\text{Disk}}^{(n+1)}$ into the step (i) as the initial guess for the next iteration.

In the step (iii) and (iv), we set $\rho_0 = 0$ in the regions at which $\ln H(r, \theta) \leq 0$.

Steps (i)-(v) are repeated until numerical values of physical quantities converge. In particular, we use the following convergence criteria

$$\left| \frac{\max(Q^{(n+1)} - Q^{(n)})}{\max(Q^{(n)})} \right| < \Delta \quad (39)$$

with $\Delta = 10^{-9}$ for a physical quantity $Q(r, \theta)$. The criteria (39) is applied to the metric functions $\varrho, \gamma, \omega, \alpha$ and the rest energy density ρ_0 . Computation is terminated if code fails or the number of iterations exceeds $N_{\text{max}} = 2000$.

Before entering the cycle of iterations (i)-(v) for the first time, we start with a value of W_{in} very close to the minimum value of $W_{\text{eq}}(r)$ to converge to a solution with a disk of a very small mass first. Then the value of $W_{\text{in}} - W_{\text{center}}$ is increased by a small increment to perform another set of iterations until the solution converges to a new state with a slightly larger disk mass. In other words, we start with a light disk and use it as an initial guess (seed solution) for a heavier disk progressively. By repeating this procedure, a sequence of numerical models with increasing disk mass can be obtained. Our strategy outlined above requires multiple rounds of iterations to reach a model with a massive disk, starting from and iterating through the ones with a lighter disk. While directly approaching to a single point chosen in the parameter space can be seemingly computationally more efficient, we have empirically observed that if the resulting disk is too massive, iterations become quickly unstable and fail within few cycles.

Table 2 summarizes the set of parameters specifying a single equilibrium solution in our scheme.

3.2 Bounds on disk rotation parameters

Specification of the rotation law in Eq. (38) with a boundary condition uniquely determines a configuration of the disk. In this section, we describe our strategy for choosing a viable set of disk rotation parameters (κ, a) and W_{in} .

It is expected that, as the mass of the disk becomes comparable with the neutron star, the disk begins to manifest its self-gravity. An equilibrium solution will start to nonlinearly deviate from a simple superposition of a rotating neutron star model with a non-self-gravitating disk. On the other hand, in the $M_{\text{Disk}} \ll M_{\text{NS}}$ limit, the

² While $l_{\text{eq}}(r)$ is given as a continuous function by Eq. (38), values of g_{tt} , $g_{t\phi}$, and $g_{\phi\phi}$ are given discretely on the grid points on the equatorial plane. We employ cubic Hermite spline to interpolate metric coefficients in the root finding.

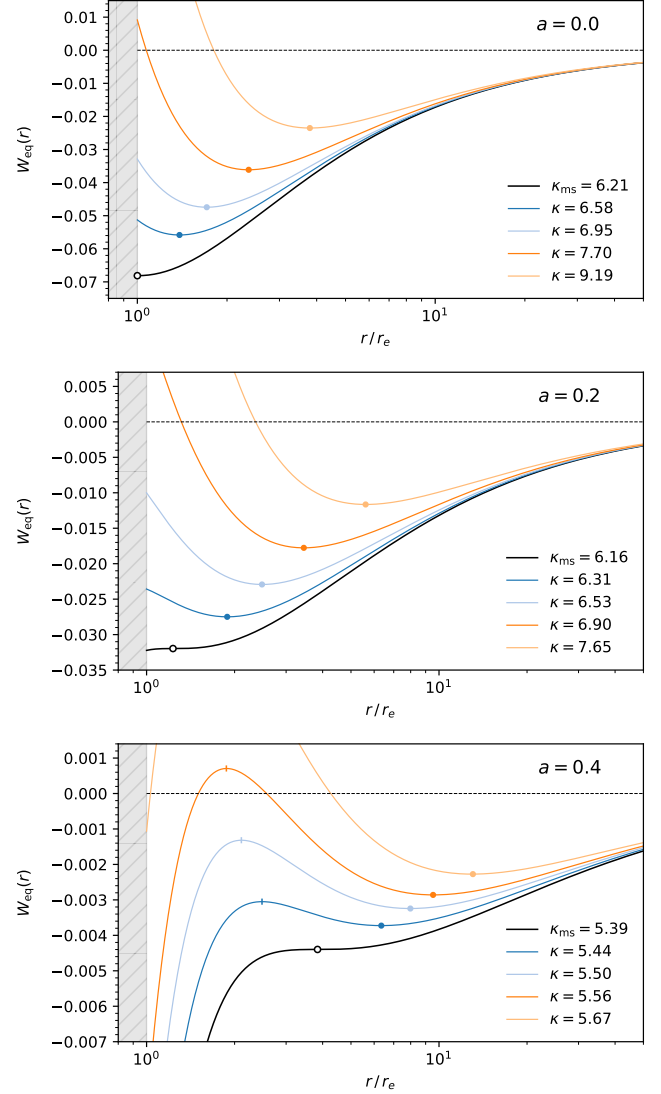


Figure 2. Variation of the effective potential $W_{\text{eq}}(r)$ with the disk rotation constant κ and the power index a . The background spacetime is a rotating neutron star model with the maximum rest energy density $\rho_0^{\text{max}} = 2.0 \times 10^{-3}$ and the axis ratio $r_p/r_e = 0.60$. In each panel, we show all types of stationary points $dW_{\text{eq}}/dr = 0$ on curves: center with a filled dot (\bullet), inflection point with an empty dot (\circ), and cusp with a short vertical line ($|$) if present.

equilibrium solution approaches a non-self-gravitating added on top of a rotating neutron star solution, with a negligible contribution to the overall spacetime geometry. The latter is a regime where the analytic theory of a non-self-gravitating disk (e.g. Fishbone & Moncrief 1976; Abramowicz et al. 1978) is applicable, neglecting the contribution of $T_{\text{Disk}}^{\mu\nu}$ in field equations.

As described in Sec. 3.1, our method of constructing a star-disk model begins with preparing an equilibrium solution of an isolated rotating neutron star and superposing a very small disk on top of it. This small disk is located at the local minimum (center) of the effective potential $W_{\text{eq}}(r)$. Before we proceed with performing iterations to find an equilibrium solution for star-disk, investigating the behavior of the effective potential $W_{\text{eq}}(r)$ with different disk rotation parameters κ and a can provide insights into a generic trend in self-gravitating solutions.

For a disk with a closed surface to exist, the effective potential

$W(r, \theta)$ needs to have a local minimum outside $r = r_e$. In Figure 2, we show how the effective potential $W_{\text{eq}}(r)$ varies with the disk rotation constant κ and the power index a . The background spacetime is an isolated rotating neutron star model with the maximum rest energy density $\rho_0^{\text{max}} = 2.0 \times 10^{-3}$ and the axis ratio $r_p/r_e = 0.60$. Following the classification in [Font & Daigne \(2002\)](#), we identify three types of stationary points at which $dW_{\text{eq}}/dr = 0$:

- Center ($d^2W_{\text{eq}}/dr^2 > 0$, local minimum),
- Cusp ($d^2W_{\text{eq}}/dr^2 < 0$, local maximum),
- Inflection point ($d^2W_{\text{eq}}/dr^2 = 0$).

These points are also displayed in Figure 2 with different marker symbols. Note that $l_{\text{eq}} = l_K$ at these stationary points.

Some qualitative observations can be made from Figure 2. First, the cusp and inflection points are not present for constant-angular momentum disks ($a = 0.0$) and begin to appear at a higher value of a . Next, the effective potential $W_{\text{eq}}(r)$ becomes more flat and shallow with higher a . Note that the Keplerian specific angular momentum l_K asymptotically approaches to $a = 0.5$ as $r \rightarrow \infty$, at which $W_{\text{eq}}(r)$ converges to a horizontal flat curve. Finally, the overall shape of $W_{\text{eq}}(r)$ changes more sensitively with respect to κ for higher a . These trends can be compared with a black hole spacetime in which the cusp is present even with constant angular momentum ($a = 0$) disk (e.g. see [Font & Daigne 2002](#)).

If κ is too small, the effective potential does not feature a center and it is not possible to construct a small disk as an initial guess (recall that our approach begins to construct a disk with a very small mass and moves to progressively larger masses). In contrast, if κ is too large, the disk will be located very far away from the neutron star and the model may be of little astrophysical interest. To this end, we choose to consider κ within the interval

$$\kappa \in [\kappa_{\text{ms}}, \kappa_c]. \quad (40)$$

The lower bound κ_{ms} ³ is found by investigating the range of κ for which the effective potential $W_{\text{eq}}(r)$ has a center within $r_e < r < \infty$. If an inflection point exists for some value of κ (middle and lower panel of Figure 2), we adopt it as κ_{ms} . If an inflection point does not exist, κ_{ms} equals the value of κ at which the center is located at $r = r_e$ ⁴ (top panel of Figure 2). In practice, κ_{ms} can be determined by picking an initial value of κ possessing a center in the corresponding $W_{\text{eq}}(r)$ and gradually decreasing κ until no center is found in $r > r_e$.

The upper bound κ_c in (40) is simply set with the condition $l_{\text{cr}}(r_e) = l_{\text{eq}}(r_e)$:

$$\kappa_c = \left(\frac{g_{t\phi} + \sqrt{g_{t\phi}^2 - g_{tt}g_{\phi\phi}}}{-g_{tt}} \right)_{r=r_e, \theta=\pi/2}. \quad (41)$$

Empirically we find that Eq. (41) serves as a reasonable upper cutoff for the parameter space of our interest, and provides a practical estimate on how much the constant κ needs to be varied to modify the configuration of the disk.

3.3 Parametrization of disk mass

In the step (iv) described in Sec. 3.1, the location of the inner edge of the disk needs to be specified during iterations either in terms of W_{in}

or r_{in} . This amounts to controlling the maximum rest energy density of the disk, which is determined from

$$W_{\text{in}} - W_{\text{center}} = \ln[\max(H_{\text{Disk}})]. \quad (42)$$

For the iterative procedure to stably converge to a solution, we need a parameter that can robustly represent the value of W_{in} . While directly controlling the value of W_{in} or r_{in} seems to be the most straightforward and intuitive, we empirically find that fixing those quantities during iterations often led to slow convergence or development of numerical instabilities. We attempt to give a plausible explanation for this in Sec. 4.

Alternatively, we parameterize the ‘depth’ of the disk in terms of a parameter $w \in [0, 1]$ defined as

$$W_{\text{in}} = (1 - w)W_{\text{center}} + wW_c \quad (43)$$

where the upper bound W_c is defined by

$$W_c \equiv \begin{cases} \max[W_{\text{cusp}}, \min(W(r = r_e), 0)], & \text{if cusp exists} \\ \min[W(r = r_e), 0], & \text{otherwise} \end{cases} \quad (44)$$

The disk depth parameter⁵ w is fixed during iterations and can be used to control the mass of the disk. Having $w > 1$ may result in either an open (infinite) disk or the disk being overfilled and exchanging pressure gradient with the neutron star. We do not consider such complications here and only consider equilibrium solutions with two separate fluid bodies. We still allow some special cases where the surfaces (at which $\log H = 0$) of the neutron star and the disk exactly touch each other, since such a configuration does not disturb each of their hydrodynamic equilibria: see Sec. 4 for examples.

3.4 Grid structure and discretization

While the original KEH scheme used a truncated computational domain with a finite radial extent, it is possible to compactify the spatial domain $r \in [0, \infty)$ into a finite interval by introducing an appropriate coordinate transformation ([Cook et al. 1992](#)). We define the radial coordinate variable $s(r) \in [0, s_{\text{max}}]$ as

$$\frac{r}{r_e} = \begin{cases} s & \text{if } 0 \leq s \leq s_0 \\ s_0 + \sigma \tan\left(\frac{\pi}{2} \frac{s - s_0}{s_{\text{max}} - s_0}\right) & \text{if } s_0 < s \leq s_{\text{max}} \end{cases} \quad (45)$$

with $s_0 = 1.0$ and $s_{\text{max}} = 4.0$. The factor σ is chosen as

$$\sigma = \frac{2}{\pi}(s_{\text{max}} - s_0) \quad (46)$$

in order to make the coordinate derivative dr/ds continuous at the matching point $s = s_0$. Compared to the coordinate transformation $r/r_e = s/(1 - s)$ introduced by [Cook et al. \(1992\)](#), our radial coordinate map in Eq.(45) places a larger portion of grid points to the outer region $r > r_e$ to resolve the structure of the disk.

Grid points are uniformly spaced in terms of the radial coordinate variable s and the angular coordinate variable $\mu = \cos \theta$. For integrating field equations we use the summation cutoff $L_{\text{max}} = 20$ in the expansion series of Green’s functions; see Eq. (33)-(35) of [Komatsu et al. \(1989a\)](#). We use the second-order discretization of spatial derivatives.

³ The subscript stands for ‘marginally stable’ ([Font & Daigne 2002](#)).

⁴ The center is a stable point ($d^2W_{\text{eq}}/dr^2 > 0$) in this case, but we will use the same symbol κ_{ms} for it.

⁵ The δ parameter defined and used in [Corvino \(2009\)](#); [Giacomazzo & Perna \(2012\)](#) has the same role, despite a slightly different form of definition.

Table 3. Convergence test on the neutron star-disk equilibrium model with the maximum rest energy density $\rho_0^{\max} = 1.0 \times 10^{-3}$, neutron star axis ratio $r_p/r_e = 0.60$, constant angular momentum disk ($a = 0.0$) with $\kappa = 7.00$, and the disk depth $q_w = 0.90$. Each column shows the coordinate radius of the neutron star r_e , the angular velocity of the neutron star Ω_0 , rest mass of the neutron star M_{NS} , rest mass of the disk M_{Disk} , and the total angular momentum of disk J_{Disk} for different grid resolutions.

Grid resolution ($N_s \times N_\mu$)	r_e	$\Omega_c (\times 10^{-2})$	M_{NS}	$M_{\text{Disk}} (\times 10^{-1})$	$J_{\text{Disk}} (\times 10^{-1})$
401 \times 201	12.098797070	2.3181343763	1.6639595312	1.0158858833	7.0040203199
801 \times 401	12.099753746	2.3180761808	1.6641761685	1.0106603325	6.9679129641
1601 \times 801	12.099821357	2.3180895689	1.6642203837	1.0097617642	6.9617026170
Convergence order	3.8	2.1	2.3	2.5	2.5

3.5 Code tests

To validate our code for the rotating neutron star, we compare the total rest (baryon) mass (M_0)

$$\begin{aligned}
 M_0 &= \int \rho_0 u^t \sqrt{-\det g} d^3x, \\
 &= \int \frac{\rho_0}{\sqrt{1-V^2}} e^{2\alpha+(\gamma-\varrho)/2} r^2 \sin\theta dr d\theta d\phi
 \end{aligned} \quad (47)$$

and angular momentum (J)

$$\begin{aligned}
 J &= \int T_\phi^t \sqrt{-\det g} d^3x \\
 &= \int \frac{(\rho_0 + \rho_i + p)V}{1-V^2} e^{2\alpha+(\gamma-\varrho)/2} r^3 \sin^2\theta dr d\theta d\phi
 \end{aligned} \quad (48)$$

with those from several available literature. Specifically, we compare our results with those presented in [Nozawa et al. \(1998\)](#), which conducted a detailed comparison between three different numerical schemes ([Komatsu et al. 1989a](#); [Stergioulas & Friedman 1995](#); [Bonazzola et al. 1993](#)) devised for rotating neutron star models. We check the values of $\bar{M}_0 \equiv K^{-1/2(\Gamma-1)} M_0$ and $\bar{J} \equiv K^{-1/(\Gamma-1)} J$ computed with the grid resolution $(N_s, N_\mu) = (401, 201)$, and our code shows a good agreement ($\lesssim 1\%$) with the results presented in [Nozawa et al. \(1998\)](#). See Appendix A for detailed comparisons.

For models with a self-gravitating disk, we check the convergence of physical quantities with increasing spatial grid resolutions. We consider a model with neutron star parameters $(\rho_0^{\max}, r_p/r_e) = (1.0 \times 10^{-3}, 0.60)$, disk rotation parameters $(\kappa, a) = (7.00, 0.0)$, and the disk depth $q_w = 0.90$ as a testing case.

Convergence test results are shown in Table 3. We increase the grid resolution by a factor of two, and measure the relative convergence order with the formula $\mathcal{O} \equiv \log_2(|q_L - q_M|/|q_M - q_H|)$, where $q_{\{L, M, H\}}$ is a physical quantity computed with the grid resolution L (low), M (medium), or H (high). The measured order of convergence is consistent with the second-order spatial discretization we used.

From Table 3, it can be seen that the difference in physical quantities between grid resolutions is larger for the disk (e.g. M_{Disk}) compared to those of the neutron star (e.g. M_{NS}). This lower accuracy can be attributed to two reasons. First, in the KEH scheme, solving the field equations is done by using Green's functions expansion at $r = 0$, which has a slower convergence of the series if $r \gtrsim r_e$. Second, the coordinate map (45) places radial grids with larger spacings in the region $r/r_e > 1$, which leads to a larger truncation error.

4 RESULTS

Our numerical model requires five parameters listed in Table 2. Rather than varying all those parameters in an equal manner, we consider a relatively limited number of neutron star configurations to focus on exploring various species of the self-gravitating disk.

We consider the maximum rest mass density⁶ $\rho_0^{\max} = 1.0 \times 10^{-3}$ (which equals $6.17 \times 10^{14} \text{g cm}^{-3}$ in the physical unit) and consider two different neutron star axis ratios: slowly rotating ($r_p/r_e = 0.999$) and rapidly rotating ($r_p/r_e = 0.60$) cases. Additionally, we also consider a rapidly rotating case with a higher central density $(\rho_0^{\max}, r_p/r_e) = (2.0 \times 10^{-3}, 0.60)$ to qualitatively study the effect of neutron star mass on disk configurations. On rotation of the disk, we only consider the prograde rotation ($\kappa > 0$) with constant ($a = 0$) and sub-Keplerian ($a = 0.4$) angular momentum distribution on the equatorial plane.

A simple $K = 100$, $\Gamma = 2$ polytrope is used for modeling the neutron star. For the matter constituting the equilibrium disk, we model it with the relativistic electron degeneracy pressure; $K = 1.18 Y_e^{4/3}$ with $Y_e = 0.5$ and $\Gamma = 4/3$ ([Font & Daigne 2002](#); [Daigne & Font 2004](#)).

All computations were performed with the grid resolution $(N_s, N_\mu) = (801, 401)$. The relative disk depth parameter w is increased with a fixed numerical increment $1/100$ during the construction of model sequences.

4.1 A representative example

Figure 3 illustrates our strategy of constructing a sequence of equilibrium models for the parameters $\rho_0^{\max} = 1.0 \times 10^{-3}$, $r_p/r_e = 0.6$, $\kappa = 7.78$, $a = 0.0$ following the computational procedure described in Sec. 3.1. We fix the disk depth parameter w in each set of iterations to converge to a single equilibrium model, then proceed to the next solution with a larger disk mass by using a slightly increased w that is fixed in the next set of iterations. We show four equilibrium models with increasing values of w in Figure 3, including a critical model (at the bottom of the figure) beyond which our code failed to converge. We note that open disks with infinite mass shown in ([Font & Daigne 2002](#)) no longer exist for the self-gravitating cases.

Effects of the self-gravity of the disk can be clearly seen through the nonlinear distortion of $W_{\text{eq}}(r)$ curves, shown in the right panels of Figure 3. The potential dip gets deepened within the interior of the disk, which is a clear indication of the disk self-gravity being non-negligible compared to the background fields from the neutron star only. The center of the disk r_c remains almost unchanged until it is eventually shifted slightly inward when the disk mass is large enough ($M_{\text{Disk}} \gtrsim 0.5$). The outer edge of the disk r_{out} rapidly increases at a lower disk mass, while it turns around and starts to move inward once the disk mass is sufficiently large. Beyond this turning point of r_{out} ,

⁶ Our code implementation does not enforce ρ_0^{\max} to be the rest mass density at the center of the neutron star, but we did not find any cases in which the maximum value of the rest mass density appears other than at the grid origin $r = 0$. This is no longer true for neutron star models with more realistic, differential rotation profiles (e.g. [Uryū et al. 2017](#)).

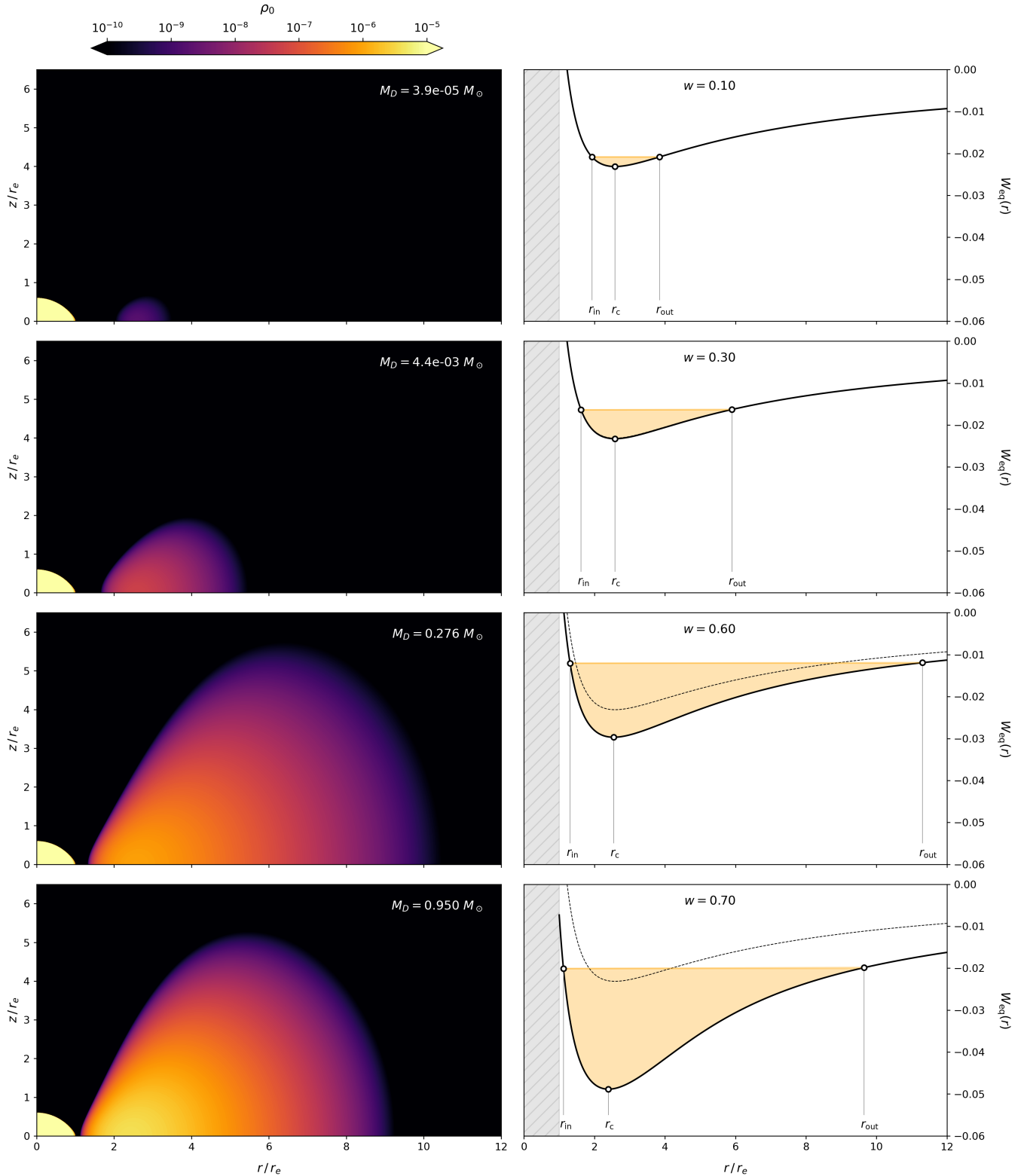


Figure 3. Illustration of the computational procedure described in Sec. 3.1 with the maximum rest mass density $\rho_0^{\max} = 1.0 \times 10^{-3}$, neutron star axis ratio $r_p/r_e = 0.60$, disk rotation parameters $\kappa = 7.78$ and $a = 0.0$. We show rest mass density on the meridional plane (left panels) and the effective potential on the equatorial plane $W_{\text{eq}}(r)$ (right panels) for increasing values of w from top to bottom. By controlling the parameter w , rest mass of the disk M_{Disk} can be increased up to a critical configuration $M_{\text{Disk}} = 0.95M_{\odot}$ (bottom). In the right panels, we show the locations of the inner edge of the disk r_{in} , center of the disk r_c , and outer edge of the disk r_{out} . The interior of the neutron star ($r < r_e$) is shown with a gray shade and the interior of the disk ($W_{\text{eq}}(r) < W_{\text{in}}$) is shown with an orange shade.

Table 4. Selected list of computed models and their parameters. ρ_0^{\max} is the maximum rest mass density, r_p/r_e is the neutron star axis ratio, and (κ, a) are rotation parameters in the angular momentum profile Eq. (38) of the disk. Computed physical quantities are the rest mass of the neutron star M_{NS} , the coordinate radius of the neutron star r_e , the coordinate rotation period of the neutron star $T_{\text{NS}} = 2\pi/\Omega_0$, and the total rest mass of the disk M_{Disk} . We also show r_{in} , r_{center} , and r_{out} , which are locations of the inner edge, center, and the outer edge of the disk on the equatorial plane in the unit of the neutron star coordinate radius r_e . For each set of the model parameters $(\rho_0^{\max}, r_p/r_e, \kappa, a)$, we show in this table an equilibrium solution with the maximum disk mass with the outer edge of the disk not exceeding $r_{\text{out}} = 20r_e$.

ρ_0^{\max} [g cm ⁻³]	r_p/r_e	κ	a	M_{NS} [M_{\odot}]	r_e [km]	T_{NS} [ms]	M_{Disk} [M_{\odot}]	r_{in} [r_e]	r_{center} [r_e]	r_{out} [r_e]	Name	Figure		
6.17×10^{14}	0.999	-	-	1.354	12.8994	23.4173	-	-	-	-				
		5.31	0.0	1.354	12.8985	25.0266	1.00×10^{-3}	1.00	1.64	3.59	A1	4a		
		5.52		1.353	12.8882	172.513	1.67×10^{-2}	1.00	1.86	6.18	A2	4b		
		6.20		1.353	12.8751	118.016	5.97×10^{-2}	1.39	2.62	10.9	A3	4c		
		7.30		1.353	12.8525	44.2607	0.199	2.04	3.97	19.6	A4			
	0.600	-	-	1.665	17.9244	1.3312	-	-	-	-	-			
		6.62	0.0	1.665	17.9197	1.3316	5.66×10^{-3}	1.00	1.67	4.06	B1	5a		
		7.40		1.661	17.5401	1.3566	0.760	1.00	2.14	9.14	B2	5b		
		7.88		1.662	17.4585	1.3617	1.02	1.14	2.46	9.65	B3	5c		
		9.62		1.665	17.8316	1.3375	0.398	2.17	4.23	18.7	B4			
		5.39	0.4	1.665	17.9244	1.3312	1.68×10^{-5}	1.72	4.50	11.5	C1	7a		
		5.42		1.665	17.9244	1.3312	2.44×10^{-4}	1.93	5.11	19.2	C2	7b		
		5.51		1.665	17.9244	1.3312	7.09×10^{-5}	3.54	6.98	19.6	C3	7c		
		1.23×10^{15}	-	-	2.024	14.2507	0.943	-	-	-	-	-		
			6.95	0.0	2.024	14.2450	0.944	7.40×10^{-3}	1.00	1.71	4.14	D1	6a	
			7.48		2.022	14.0351	0.954	0.419	1.00	2.08	8.60	D2	6b	
7.70			2.022	13.9675	0.958	0.586	1.07	2.23	9.04	D3				
8.22			2.023	14.1591	0.948	0.242	1.46	2.79	11.0	D4	6c			
5.42	0.4		2.024	14.2507	0.943	1.05×10^{-7}	2.81	5.45	8.86	E1	8a			
5.44			2.024	14.2507	0.943	1.46×10^{-5}	2.49	6.35	15.2	E2	8b			
5.50			2.024	14.2507	0.943	3.65×10^{-5}	4.03	7.98	19.6	E3	8c			

the radial extent and thickness of the disk do not change significantly, or even shrink in size (bottom panels of Figure 3).

With the example presented in Figure 3, we now revisit the issue of parametrizing disk mass discussed in Sec. 3.3. From the top and bottom panels of Figure 3, it can be seen that the disk in both models, despite their large difference in mass, shows approximately the same values of $W_{\text{in}} \approx -0.02$. This degeneracy indicates that a single value of W_{in} does not always correspond to a unique configuration of the disk, showing its inadequacy as a parameter for controlling the mass of the disk. Location of the inner edge of disk r_{in} exhibits a monotonic decrease with increasing disk mass, but a steep slope of $W_{\text{eq}}(r)$ developing near $r \rightarrow r_e$ makes it numerically challenging to find an optimal size of increment that can keep iteration processes stable. In these regards, the method of parametrization (43) shows less problematic behavior and provides a more robust way to control the disk mass in actual computations.

4.2 Equilibrium Models

Table 4 summarizes the parameters of and the resulting physical quantities from a selected list of models.

Some models exhibit a radially extended disk with its outer edge reaching up to ~ 200 km. As discussed in Sec. 3.5, the accuracy of the result can be significantly lost if the radial extent of the disk is too large. The radial grid resolution $N_s = 801$ used in computation, in combination with the radial coordinate map (45) used in this work, places only ~ 40 grid points within $r \in (20r_e, \infty)$, putting the validity of a numerical solution in question. For these reasons, models with $r_{\text{out}} > 20r_e$ are discarded from the results.

Each of the entries in Table 4 is understood as that a continuous

sequence of models can be obtained up to the value presented in the table, at which the model is either at a critical rotation or the outer edge of the disk reached $r_{\text{out}} \leq 20r_e$. For instance, the entry B2 (corresponding to Figure 5b) indicates that all configurations with $M_{\text{Disk}} \leq 0.76M_{\odot}$ could have been obtained with the given parameters $\rho_0^{\max} = 1.0 \times 10^{-3}$, $r_p/r_e = 0.60$, $\kappa = 7.40$, and $a = 0.0$.

Several generic trends in physical quantities can be observed from Table 4, by comparing results with those without self-gravity of the disk. As the mass of the disk gets larger, the rest mass of the neutron star decreases by a small amount ($\lesssim 0.1\%$). The coordinate radius of the neutron star is also decreased with a slightly larger amount. The neutron star also shows slower rotation when the disk exists.

This can be qualitatively understood as the gravitational pull from the disk, pointing radially outward on the equatorial plane, provides extra centrifugal support to the rotating matter inside the neutron star. Therefore, with fixed maximum rest mass density and axis ratio, the matter distribution of the neutron star is changed into a configuration with a slower rotation, resulting in a smaller mass, smaller size, and a slower rotation frequency. In particular, the gravitational effect from the disk is quite noticeable in the cases with a slowly rotating ($r_p/r_e = 0.999$) neutron star, significantly increasing its rotation period while leaving the rest mass and the coordinate radius almost unchanged. On the contrary, the effects on the rotation frequency of the neutron star are marginal for rapidly rotating ($r_p/r_e = 0.60$) cases. Overall, these trends found in our results are also consistent with the findings of Nishida et al. (1992).

We look into details of the numerical models with a constant angular momentum disk (model A, B, D) in Sec. 4.2.1, then we discuss the qualitative effect of higher disk rotation index a (model C, E) in Sec. 4.2.2.

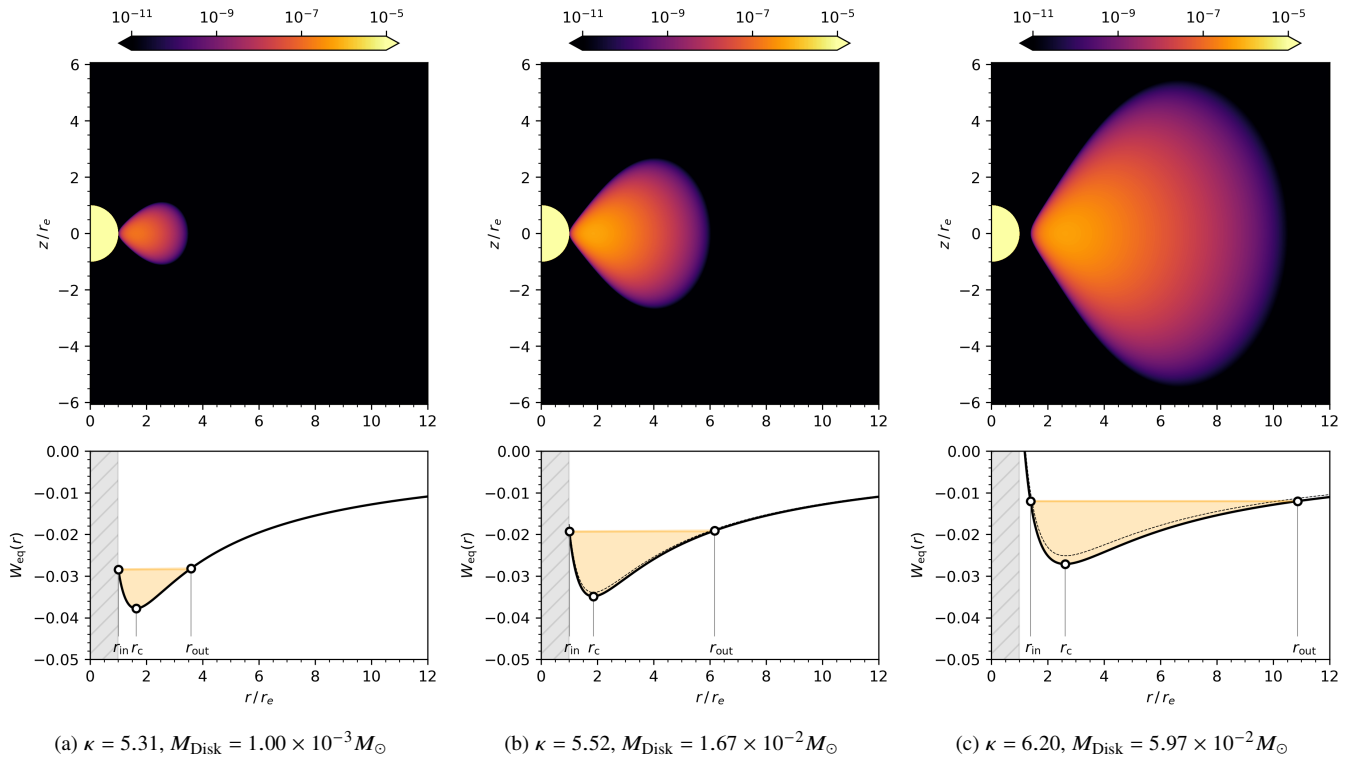


Figure 4. Self-gravitating star-disk models for $(\rho_0^{\text{max}}, r_p/r_e) = (1.0 \times 10^{-3}, 0.999)$ neutron star with a constant angular momentum disk ($a = 0.0$). Equilibrium solutions with three values of κ are shown: disk can be filled to $w = 1.0$ but self-gravity is still nearly negligible (left); the disk can be filled up but the effect of self-gravity becomes noticeable (center); the disk reaches a detached critical configuration ($r_e < r_{\text{in}}$) with non-negligible self-gravity (right). *Upper panels:* Rest mass density ρ_0 on the meridional plane. *Lower panels:* Effective potential $W_{\text{eq}}(r)$ is shown with a thick black line, and the potential without the disk self-gravity is shown with the dotted line. We mark the locations of the inner edge, center, and outer edge of the disk with circles, and display the interior of the disk with a yellow shade. Interior of the neutron star is shown with a grey shade.

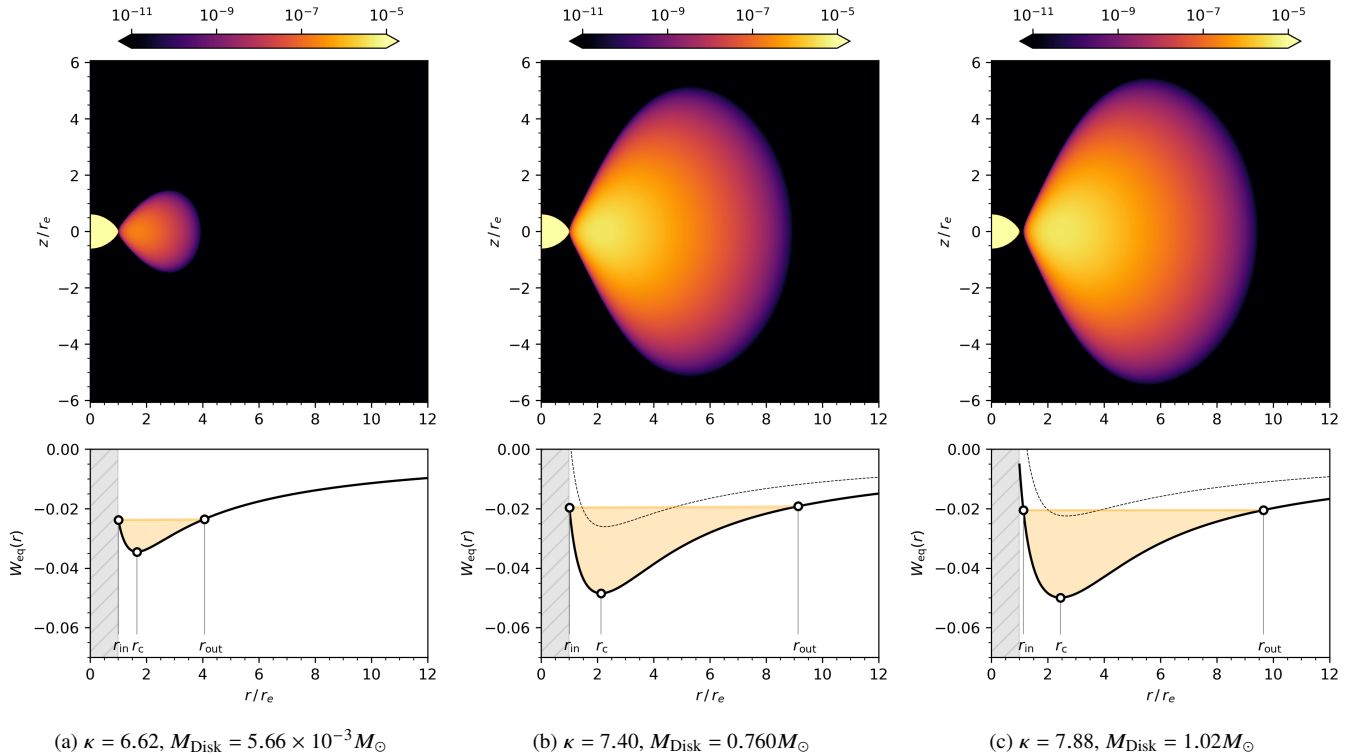


Figure 5. Same as Figure 4, for rapidly rotating case $r_p/r_e = 0.60$.

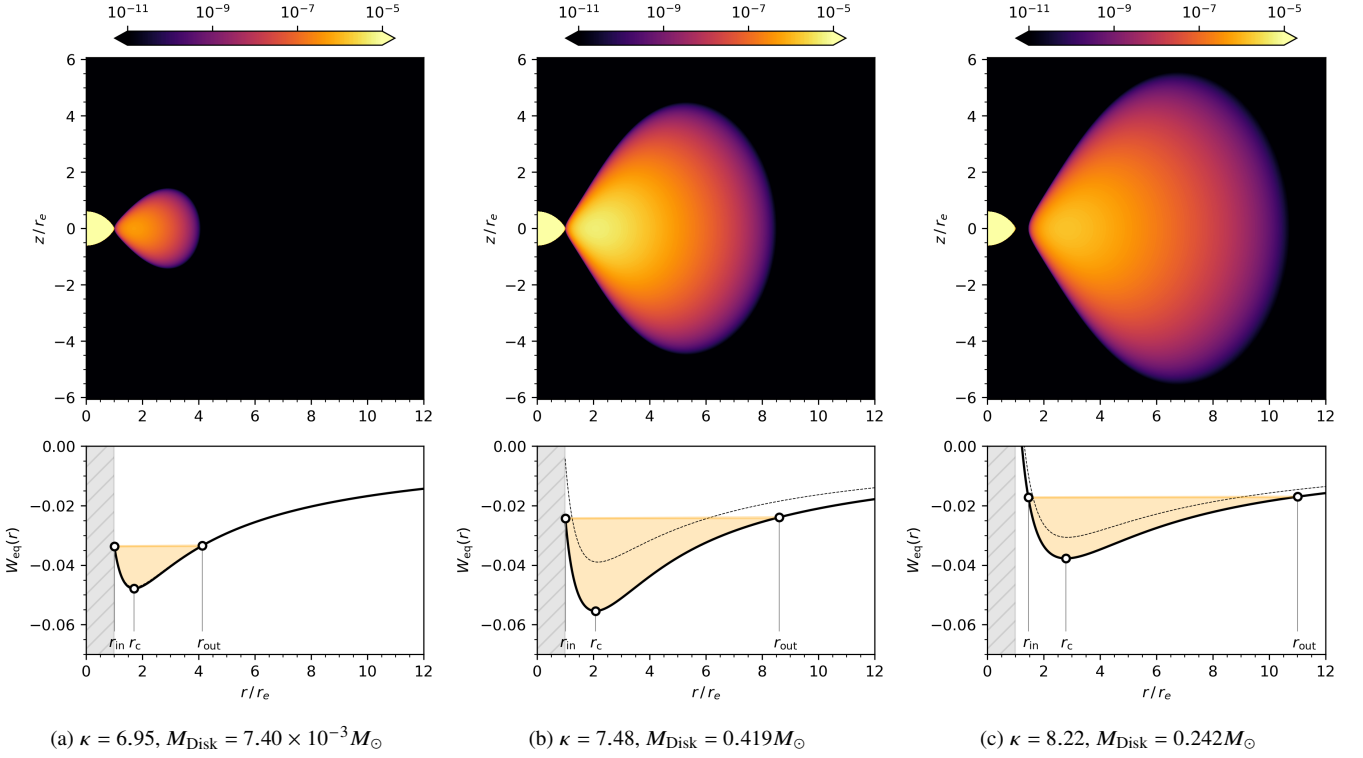


Figure 6. Same as Figure 5, for a higher maximum rest mass density $\rho_0^{\text{max}} = 2 \times 10^{-3}$.

4.2.1 Constant angular momentum disk

Figure 4 shows the rest mass density on the meridional plane for models involving a slowly rotating ($r_p/r_e = 0.999$) neutron star with $\rho_0^{\text{max}} = 1.0 \times 10^{-3}$ and a constant angular momentum disk (models A1-A3). Three selected values of κ correspond to the configuration at which: (i) the disk is located close and can be filled up to $w = 1$, touching the neutron star surface but its self-gravity is not significant (model A1, Figure 4a); (ii) same as the first case but the self-gravity is non-negligible (model A2, Figure 4b); (iii) the inner edge of the disk being detached from the neutron star surface, cannot be fully filled ($w < 1$), and the self-gravity is non-negligible (model A3, Figure 4c). In the last case, the model reaches a critically rotating state at an upper limit $w_{\text{max}} = 0.56$.

The angular velocity of the neutron star is significantly affected by the gravity from the disk; the neutron star in the model A2 shows more than seven times slower rotation than the isolated case. However, this should not be interpreted as that a rotating neutron star can actually be ‘slowed down’ to this amount by forming a disk around it, but needs to be understood as the functional dependency between the neutron star axis ratio r_p/r_e and the rotation frequency T_{NS} is very sensitive to the influence from an external gravity in a slowly rotating regime. Comparing models A1-A4, we see that the rotation speed of the neutron star is most affected in model A2 even if model A4 has more than 10 times larger disk mass. This indicates that the influence of the disk on the hydrodynamic equilibrium of the neutron star is not solely dominated by the rest mass of the disk, but its proximity to the neutron star surface also plays an important role.

We show the same set of plots for a rapidly rotating neutron star ($r_p/r_e = 0.60$) in Figure 5. These models (B1-B4), with a rapidly rotating neutron star, permits solutions with larger disk mass, even up to $M_{\text{Disk}} \approx 1.0$ (model B3, Figure 5c); note the large distortion of

the effective potential $W_{\text{eq}}(r)$. Meanwhile, the influence of the disk on the rotation period of the neutron star is small ($\lesssim 2\%$), implying that its relative contribution to the hydrodynamic equilibrium of the neutron star is much smaller than the models with a slowly rotating neutron star, as expected.

Models D1-D4 have a rapidly rotating neutron star with a higher maximum rest energy density $\rho_0^{\text{max}} = 2.0 \times 10^{-3}$; models D1, D2, and D4 are shown in Figure 6. The neutron star has a higher mass $M_{\text{NS}} \approx 2.0 M_{\odot}$, more compact radius $r_e \approx 14 \text{ km}$, and shorter rotation period $\leq 1 \text{ ms}$. This sequence yields models with the disk mass being a bit smaller than the models B1-B4.

4.2.2 Non-constant angular momentum disk

As discussed in Sec. 3.2, a higher power index a facilitates the development of a cusp in the effective potential $W_{\text{eq}}(r)$, effectively prohibiting the disk with a large mass. Our parameter study confirms that it is difficult to obtain a solution with a large disk mass; all our results show $M_{\text{Disk}} \lesssim 10^{-4} M_{\odot}$.

In Figure 7 (Figure 8), we show the rest mass density on the meridional plane and the effective potential of models C1-C3 (E1-E3). It can be seen that the cusp is present near the surface of the neutron star, and any part of the disk with its effective potential exceeding the value of W_{cusp} is not able to sustain an equilibrium but will overflow and accrete onto the neutron star. Note that the disk filling exactly up to the cusp of the potential $W_{\text{eq}}(r)$ shows a sharp and thin inner edge (e.g. Figure 7a), which conforms with the boundary of the Roche lobe.

In general, compared to the constant angular momentum disks, sub-Keplerian disk models show more “shallow and flat” curves of $W_{\text{eq}}(r)$. With a high value of a close to the Keplerian ($a = 0.5$) limit, the presence of the cusp prevents the formation of a potential ‘dip’ in

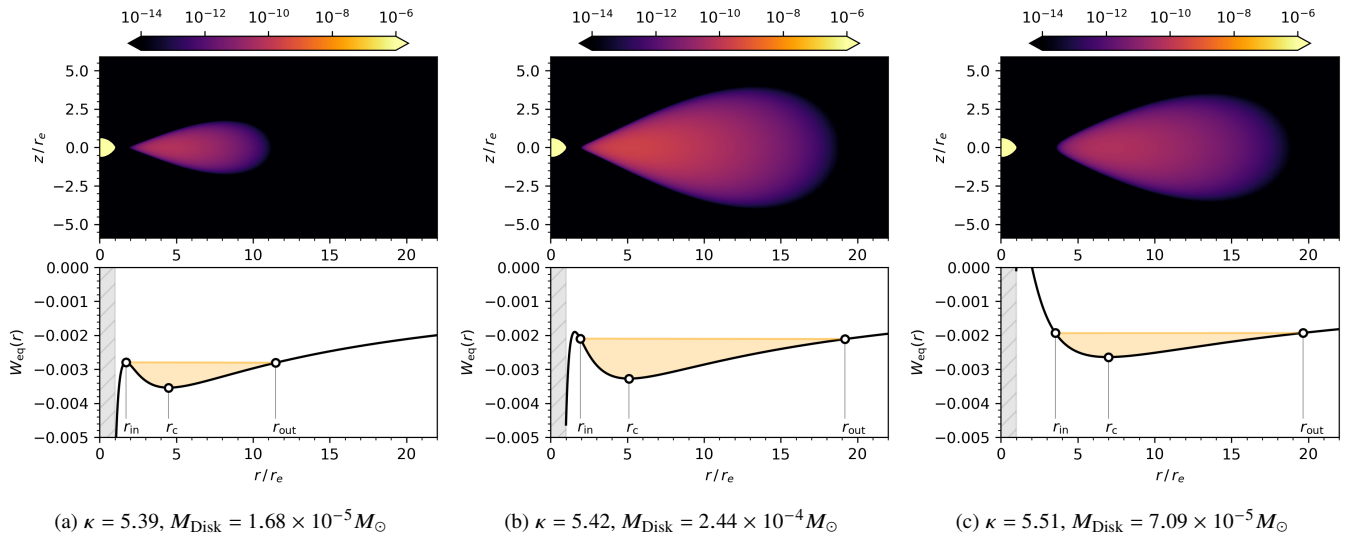


Figure 7. Non-constant angular momentum disk models. $\rho_0^{\text{max}} = 1.0 \times 10^{-3}$, $r_p/r_e = 0.60$, and $a = 0.4$

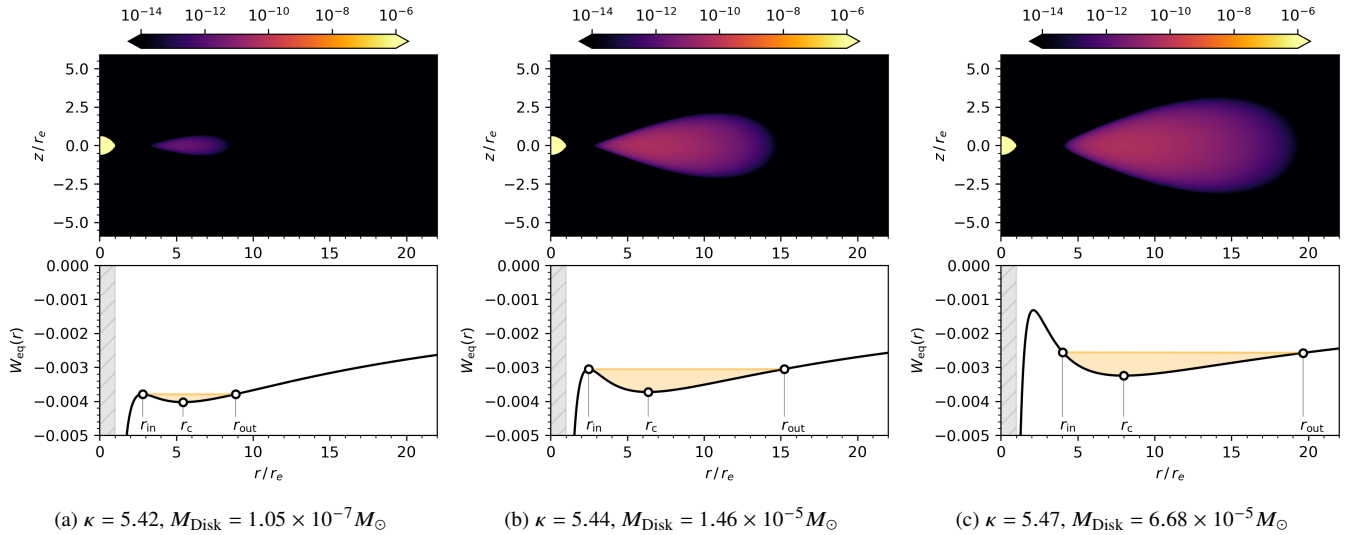


Figure 8. Same as Figure 7, for a higher maximum rest mass density $\rho_0^{\text{max}} = 2.0 \times 10^{-3}$

the W_{eq} curve. This has two consequences in equilibrium solutions, namely that (1) the mass of the disk is much smaller overall, and (2) the radial extent of the disk grows very fast with increasing disk depth parameter w . We also note that the viable range of κ in which a disk can be constructed is much narrower than the constant angular momentum cases (see Table 4).

4.3 Comparisons with non-self-gravitating disks

So far, we have mainly focused on the influence of a self-gravitating disk on the neutron star, where the matter distribution of the disk would also reorganize itself due to its self-contribution to the gravitational field. In this section, we attempt to assess the impact of the self-gravity of the disk on itself, compared to the cases in which we ignore it in calculations.

We construct an equilibrium model with $\rho_0^{\text{max}} = 1.0 \times 10^{-3}$, $r_p/r_e = 0.6$, $\kappa = 7.88$, $a = 0.0$, and $w = 0.54$, yielding the disk rest mass $M_{\text{Disk}} = 0.101 M_{\odot}$ where $M_{\text{NS}} = 1.66 M_{\odot}$. Next, using

the same set of parameters for the neutron star, we construct another equilibrium solution with a non-self-gravitating disk having the same rest mass. Figure 9 compares these two cases. The self-gravity of the disk drags the outer edge r_{out} inward while the inner edge r_{in} does not shift as much. It can be seen that the spatial distribution of the low-density outer envelope of the disk is notably compressed toward the disk center in the self-gravitating case. The difference in the coordinate radius (rest mass) of the neutron star between these two models is 0.2% (0.01%), which is very small compared to the relative change of the disk structure shown in Figure 9. Therefore, we conclude that this spatial compression of the disk is mostly, if not entirely, due to its self-gravity. The effective potential at the center of the disk W_{center} shows $\sim 10\%$ difference in the presence of the disk self-gravity, which agrees in orders of magnitude with $M_{\text{Disk}}/M_{\text{NS}} \approx 0.06$.

We show a more extreme case with $M_{\text{Disk}} = 0.97 M_{\odot}$ ($\kappa = 7.78$) in Figure 10. The difference of the neutron star between the self-gravitating and non-self-gravitating disk solutions in this case is 3%

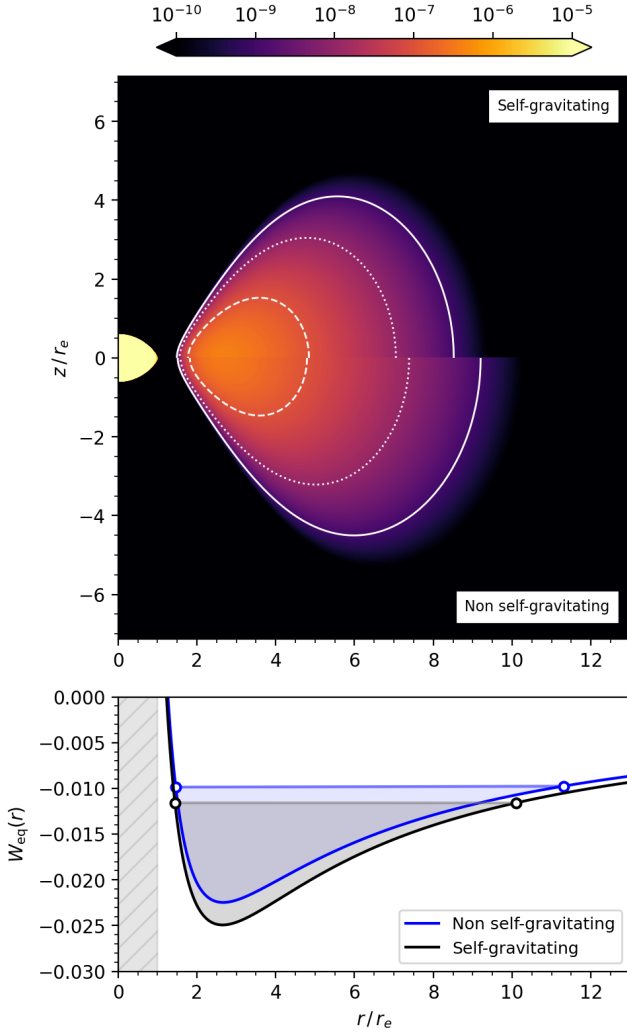


Figure 9. Comparison between models with and without the disk self-gravity for $\kappa = 7.88$, $M_{\text{Disk}} = 0.101M_{\odot}$. (Top) Rest mass density of the disk in self-gravitating and non-self-gravitating cases. To better visualize the difference of the matter distribution between two cases, we draw contour lines for $\rho_0 = 10^{-9}, 10^{-8}, 10^{-7}$ with solid, dotted, and dashed white lines, respectively. (Bottom) Effective potential $W_{\text{eq}}(r)$. The inner and outer edges of the disk are shown with small circles, and the interior region of the disk is displayed with colored shades.

in radius and 0.2% in mass, while the spatial structure of the disk undergoes a much more dramatic change. Using the same solution, Figure 11 shows the metric functions ϱ , γ , α , ω as a function of r on the equatorial plane along with the case without the disk self-gravity. Due to an increased total gravitational mass of the system, all metric functions have larger absolute values compared to the non-self-gravitating case. One exception is the frame dragging potential ω , which shows a slight increase in $r \leq 0.34r_e$. At the center of the neutron star, ϱ and α show about 7% difference, while γ and ω undergo about 8-9 times smaller changes. In terms of the relative change, both metric functions ϱ and γ show the most deviation at $r = 5.20r_e$, having as about twice as larger absolute values. The metric function α shows the maximum 70% increase in its value at $r = 5.32r_e$, where the function ω shows its maximum increase of 6.12 times at $r = 6.44r_e$. Note from Figure 10 that the center of the disk is located at $r = 2.40r_e$, which does not conform with the

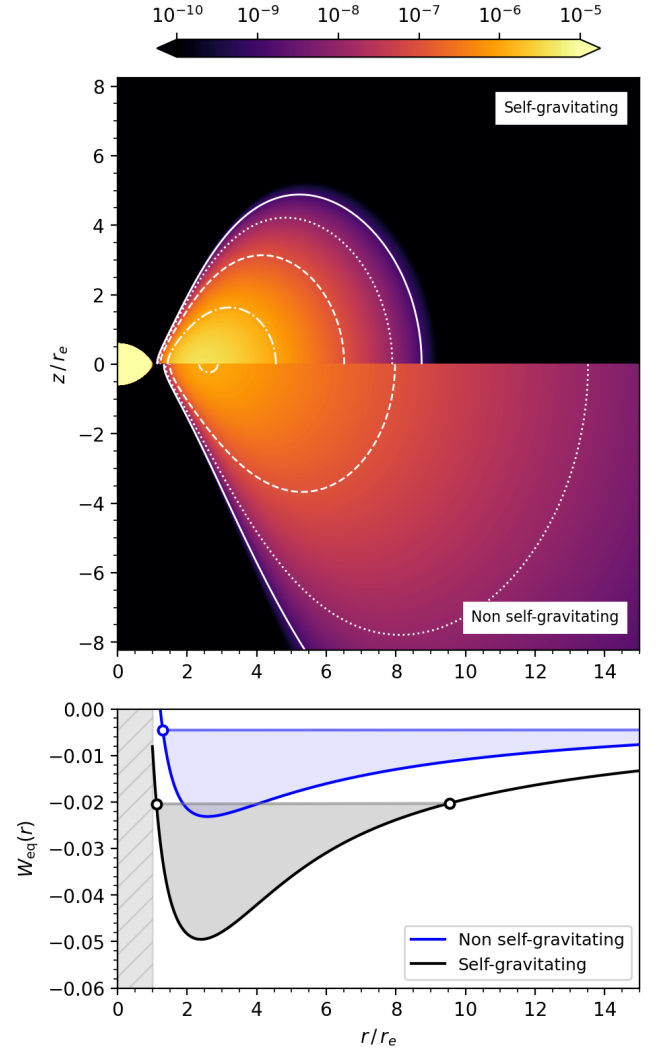


Figure 10. Same as Figure 9, with $\kappa = 7.78$ and $M_{\text{Disk}} = 0.969M_{\odot}$. In the upper panel, an additional contour level $\rho_0 = 10^{-6}$ is shown with a white dash-dotted line.

locations at which metric functions show the largest deviation from the non-self-gravitating disk model.

In Figure 12, we plot the rest mass of the disk versus the disk depth parameter w for a self-gravitating disk and a non-self-gravitating case, for $\kappa = 7.20$ and $\kappa = 7.78$ with other model parameter fixed as $\rho_0^{\text{max}} = 1.0 \times 10^{-3}$, $r_p/r_e = 0.60$, $a = 0.0$. Since a non-self-gravitating disk with $w = 1$ corresponds to an open (infinite) disk, the mass of the disk diverges as $w \rightarrow 1$ (dashed lines). The discrepancy between self-gravitating and non-self-gravitating cases is already clearly visible from $M_{\text{Disk}} \approx 0.1M_{\odot}$. A kink present on the $\kappa = 7.78$ (black solid line) plot in Figure 12 is a parametrization artifact from its definition Eq. (44). Due to the self-gravity of the disk with a large mass, $W_{\text{eq}}(r_e)$ can drop to a negative value and parametrization upper bound is changed from a fixed point (zero) to $W_{\text{eq}}(r_e)$, inducing a discontinuous jump in the slope dM_{Disk}/dw . We also note that when adopting the parametrization of the disk depth in terms of the variable w , the deviation of the mass of a self-gravitating disk from a non-self-gravitating case can be both positive or negative; a self-gravitating solution can lead to either a more massive disk or a less massive

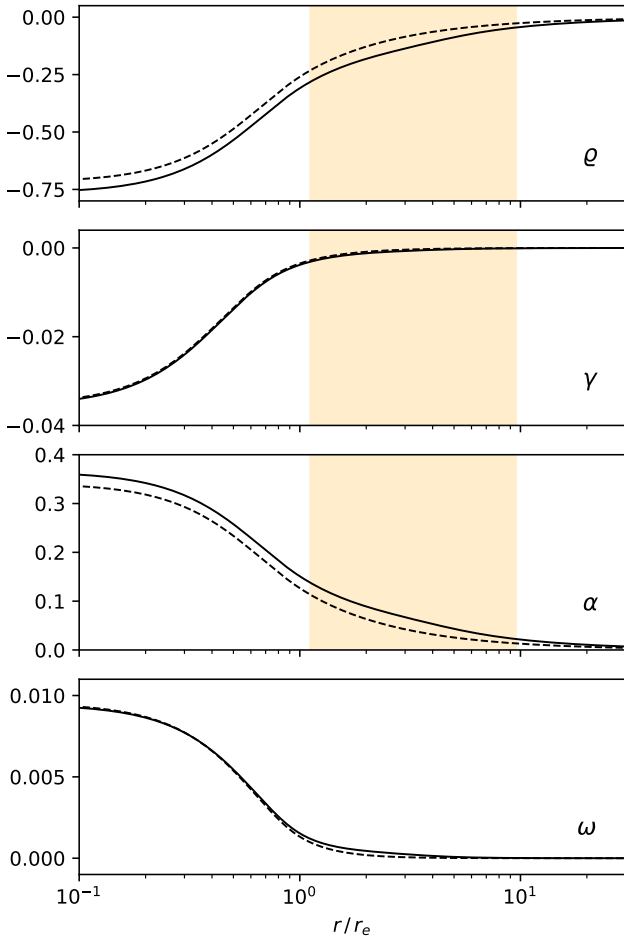


Figure 11. Comparison of the metric functions ρ , γ , α , and ω (see Eq. (1) for definition) on the equatorial plane with (solid) and without (dashed) the disk self-gravity. Interior of the neutron star and the disk are shown with gray and orange shades, respectively. Model parameters and the self-gravitating solution is same as the one shown in Figure 10.

disk, depending on other physical parameters associated with the equilibrium state.

5 SUMMARY AND CONCLUSION

Extending the scheme of [Komatsu et al. \(1989a\)](#) with an extra step constructing an equilibrium disk during iterations, we have constructed classes of numerical models describing a self-gravitating equilibrium disk orbiting around a rapidly rotating neutron star. Our formulation makes use of the specific angular momentum l —instead of the coordinate angular velocity Ω —in prescribing the rotation profile of the disk, facilitating parameter studies on the disk rotation in a more direct manner.

Since the explorable parameter space of the star-disk system is much wider than that of an isolated rotating neutron star, the scope of this paper was somewhat limited, namely assuming a uniformly rotating neutron star and the disk following the angular momentum distribution given by Eq. (38) on the equator. Despite these simplifications, several impacts of the self-gravity of the disk on the system could have been identified:

- In an equilibrium state with a given central rest mass density,

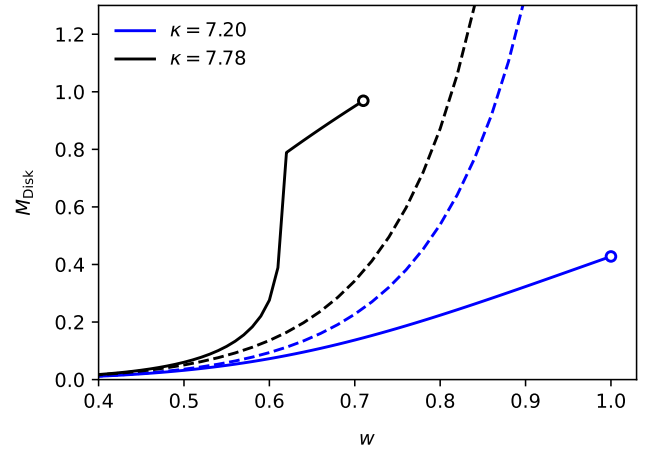


Figure 12. Rest mass of the disk (in units of the solar mass) versus the depth parameter w . Non self-gravitating disk solutions are shown with dashed lines while the self-gravitating solutions are shown with solid lines. Model parameters are $\rho_0^{\max} = 1.0 \times 10^{-3}$, $r_p/r_e = 0.60$, and $a = 0.0$. A kink of the $\kappa = 7.78$ curve near $M_{\text{Disk}} = 0.8M_{\odot}$ is a parametrization artifact; see discussions in Sec. 4.3.

the neutron star at the center decreases slightly in its mass and radius, and its rotation becomes slower. These basic findings are consistent with the results from [Nishida et al. \(1992\)](#).

- Compared to a non-self-gravitating case, the disk is radially compressed toward the star. Outer low-density regions are affected most while the change is marginal near the inner edge and the center of the disk.
- Constant angular momentum disk is preferable for the formation of a more massive and thick disk near the neutron star. Sub- or nearly-Keplerian disks in general show lower rest mass density and more extended geometry, which may make it very difficult to accurately compute an equilibrium solution for which the self-gravity of the disk is large enough.
- Roughly speaking, the self-gravity of the disk impacts its internal structure with the orders of $M_{\text{Disk}}/M_{\text{NS}}$, while little affecting the mass or radius of the neutron star.

The uniformly rotating assumption on the neutron star greatly simplifies the problem, but at the same time largely restricting us from resolving radius-dependent effects by the gravitational pull of the disk to the interior of the neutron star. A more realistic, differential rotation law (e.g. [Galeazzi et al. 2012](#); [Uryū et al. 2017](#); [Bauswein & Stergioulas 2017](#); [Bozzola et al. 2018](#); [Iosif & Stergioulas 2021](#)) can be used for an improved modeling of the rotating neutron star. Also, we only have considered a simple power law (Eq. (38)) as a representative example of a non-constant angular momentum distribution of the disk, where several alternate prescriptions are available, such as adopting a different form of angular momentum distribution ([Penna et al. 2013](#); [Qian et al. 2009](#)) or specifying a nontrivial functional relationship between the angular velocity Ω and the specific angular momentum l ([Witzany & Jefremov 2018](#); [Wielgus et al. 2015](#)). Further research with an extended set of rotation profiles of both the neutron star and the disk will allow us to examine more diverse configurations of the system.

Several potential improvements for speeding up the computational procedure (described in Sec. 3.1) can be available, such as an adaptive control of the convergence threshold Δ and the increment in the disk depth parameter w when approaching a solution, or applying the

successive over-relaxation method (Varga 2000; Hageman & Young 2004) over each iterations.

On the matter physics, further improvements can be made by using a more realistic equation of state in the typical rest mass density range of the disk observed in the current work ($\rho_0 = 10^6 - 10^{11} \text{ g cm}^{-3}$), as well as adopting a tabulated, nuclear equation of state for the neutron star rather than using a simple polytrope. The remnant of the binary neutron star merger or an accreting proto-neutron star is expected to be born hot exceeding $1 \text{ MeV} \approx 10^{10} \text{ K}$ (Bernuzzi 2020; Prakash et al. 1997; Haensel et al. 2007). A realistic equilibrium model aiming to imitate such hot accreting states needs to incorporate thermal contributions as well, for which a recently developed approach by Camelio et al. (2019, 2021) for non-barotropic equilibrium solutions can be useful.

Since our models do not take energy and pressure contributions from magnetic fields into account, they are only applicable to an unmagnetized or at most weakly magnetized system. In realistic scenarios, magnetic fields can change the equilibrium configuration (e.g. Komissarov 2006) or would trigger instabilities so that such systems evolve into accreting states. The dynamical stability of our results is still under question as well. These aspects can be further investigated by feeding our model to an evolution code as initial data and running general relativistic hydrodynamics simulations, which we aim as future work.

ACKNOWLEDGEMENTS

YK thanks to Chan Park for his assistance and comments, and is grateful to Isaac Legred and Michael Pajkos for helpful discussions. JK acknowledges that this research was supported by Basic Science Research Program through the National Research Foundation of Korea (NRF) funded by the Ministry of Education (NRF-2021R111A2050775). HIK acknowledges that this research was supported by Basic Science Research Program through the National Research Foundation of Korea (NRF) funded by the Ministry of Education through the Center for Quantum Spacetime (CQUeST) of Sogang University (NRF-2020R1A6A1A03047877). HML was supported by the NRF grant No. 2021M3F7A1082056. We acknowledge the hospitality at APCTP where part of this work was done. Computations were performed on the gmuu cluster at the Korea Astronomy and Space Science Institute. Figures in this article were produced using Matplotlib (Caswell et al. 2023), Numpy (Harris et al. 2020), and Scipy (Virtanen et al. 2020) packages. We also thank the anonymous referee for valuable comments and insightful suggestions.

DATA AVAILABILITY

The computed models which are listed in Table 4 and assigned with Figures (i.e. all entries except A4, B4, D3) are publicly available on Zenodo (Kim et al. 2024). Other data underlying this article will be shared upon request to the corresponding author.

REFERENCES

- Abbott B. P., et al., 2016, *Phys. Rev. Lett.*, **116**, 061102
- Abbott B. P., et al., 2017, *ApJ*, **848**, L12
- Abdikamalov E. B., Ott C. D., Rezzolla L., Dossart L., Dimmelmeier H., Marek A., Janka H. T., 2010, *Phys. Rev. D*, **81**, 044012
- Abramowicz M. A., 1971, *Acta Astron.*, **21**, 81
- Abramowicz M. A., 1974, *Acta Astron.*, **24**, 45
- Abramowicz M. A., Fragile P. C., 2013, *Living Reviews in Relativity*, **16**, 1
- Abramowicz M., Jaroszynski M., Sikora M., 1978, *A&A*, **63**, 221
- Ansorg M., Petroff D., 2005, *Phys. Rev. D*, **72**, 024019
- Baumgarte T. W., Shapiro S. L., 2010, *Numerical relativity: solving Einstein's equations on the computer*. Cambridge University Press, Cambridge ; New York
- Bauswein A., Stergioulas N., 2017, *MNRAS*, **471**, 4956
- Bernuzzi S., 2020, *General Relativity and Gravitation*, **52**, 108
- Blaes O. M., Arras P., Fragile P. C., 2006, *MNRAS*, **369**, 1235
- Bonazzola S., Gourgoulhon E., Salgado M., Marck J. A., 1993, *A&A*, **278**, 421
- Bozzola G., Stergioulas N., Bauswein A., 2018, *MNRAS*, **474**, 3557
- Burrows A., Vartanyan D., Wang T., 2023, *ApJ*, **957**, 68
- Camelio G., Dietrich T., Marques M., Rosswog S., 2019, *Phys. Rev. D*, **100**, 123001
- Camelio G., Dietrich T., Rosswog S., Haskell B., 2021, *Phys. Rev. D*, **103**, 063014
- Camilletti A., Perego A., Guercilena F. M., Bernuzzi S., Radice D., 2024, *Phys. Rev. D*, **109**, 063023
- Caswell T. A., et al., 2023, matplotlib/matplotlib: REL: v3.7.1, doi:10.5281/zenodo.7697899, <https://doi.org/10.5281/zenodo.7697899>
- Chakrabarti S. K., 1988, *Journal of Astrophysics and Astronomy*, **9**, 49
- Chan C., Müller B., Heger A., Pakmor R., Springel V., 2018, *ApJ*, **852**, L19
- Cook G. B., Shapiro S. L., Teukolsky S. A., 1992, *ApJ*, **398**, 203
- Cook G. B., Shapiro S. L., Teukolsky S. A., 1994a, *ApJ*, **422**, 227
- Cook G. B., Shapiro S. L., Teukolsky S. A., 1994b, *ApJ*, **424**, 823
- Corvino G., 2009, PhD thesis, Università degli studi di Parma
- Daigne F., Font J. A., 2004, *MNRAS*, **349**, 841
- Das P., Porth O., 2024, *ApJ*, **960**, L12
- Eriguchi Y., Hachisu I., Nomoto K., 1994, *MNRAS*, **266**, 179
- Fishbone L. G., Moncrief V., 1976, *ApJ*, **207**, 962
- Font J. A., Daigne F., 2002, *MNRAS*, **334**, 383
- Foucart F., 2012, *Phys. Rev. D*, **86**, 124007
- Foucart F., et al., 2016, *Phys. Rev. D*, **93**, 044019
- Fragile P. C., Ballantyne D. R., Maccarone T. J., Witry J. W. L., 2018, *ApJ*, **867**, L28
- Fryer C. L., 1999, *ApJ*, **522**, 413
- Galeazzi F., Yoshida S., Eriguchi Y., 2012, *A&A*, **541**, A156
- Giacomazzo B., Perna R., 2012, *ApJ*, **758**, L8
- Hachisu I., 1986, *ApJS*, **61**, 479
- Haensel P., Potekhin A. Y., Yakovlev D. G., eds, 2007, *Neutron Star Cores: Nucleons and Hyperons*. Springer New York, New York, NY, pp 207–280, doi:10.1007/978-0-387-47301-7_5, https://doi.org/10.1007/978-0-387-47301-7_5
- Hageman L. A., Young D. M., 2004, *Applied iterative methods*. Dover books on mathematics, Dover Publications, Mineola, N.Y
- Harris C. R., et al., 2020, *Nature*, **585**, 357
- Iosif P., Stergioulas N., 2021, *MNRAS*, **503**, 850
- Iosif P., Stergioulas N., 2022, *MNRAS*, **510**, 2948
- Kasliwal M. M., et al., 2017, *Science*, **358**, 1559
- Kim Y., Kim J., Kim H. I., Lee H. M., 2024, General relativistic self-gravitating equilibrium disks around rotating neutron stars: dataset, doi:10.5281/zenodo.13836034, <https://doi.org/10.5281/zenodo.13836034>
- Komatsu H., Eriguchi Y., Hachisu I., 1989a, *MNRAS*, **237**, 355
- Komatsu H., Eriguchi Y., Hachisu I., 1989b, *MNRAS*, **239**, 153
- Komissarov S. S., 2006, *Mon. Not. Roy. Astron. Soc.*, **368**, 993
- Kozłowski M., Jaroszynski M., Abramowicz M. A., 1978, *A&A*, **63**, 209
- Krüger C. J., Foucart F., 2020, *Phys. Rev. D*, **101**, 103002
- Lanza A., 1992, *ApJ*, **389**, 141
- Matuszková M., et al., 2024, Accretion tori around rotating neutron stars – Paper II: Oscillations and precessions (arXiv:2403.16231)
- Nishida S., Eriguchi Y., 1994, *ApJ*, **427**, 429
- Nishida S., Eriguchi Y., Lanza A., 1992, *ApJ*, **401**, 618
- Nozawa T., Stergioulas N., Gourgoulhon E., Eriguchi Y., 1998, *Astron. Astrophys. Suppl. Ser.*, **132**, 431
- Paschalidis V., Stergioulas N., 2017, *Living Reviews in Relativity*, **20**, 7

Table A1. Normalized rest mass \bar{M}_0 and total angular momentum \bar{J} for a list of neutron star models. Model names and their parameters follow the naming notation of [Nozawa et al. \(1998\)](#) so that the results can be compared with Table 1 and Table 2 therein. For the last four models, we display results with additional significant figures to compare with Table 8 and Table 9 of the reference.

Model	\bar{M}_0	\bar{J}
N05sr	1.52e-01	2.18e-03
N05rr	1.59e-01	1.07e-02
N075sr	1.60e-01	2.86e-03
N075mr	1.87e-01	1.74e-02
N10sr	1.82e-01	4.21e-03
N10rr	1.73e-01	9.49e-03
N15sr	2.08e-01	1.02e-02
N15rr	2.77e-01	2.13e-02
N15sn	9.7621e-05	3.5979e-07
N15mr	3.0421e-01	3.8759e-02
N05sn	6.2995e-08	1.3174e-13
N05mr	1.8259e-01	1.7221e-02

- Penna R. F., Kulkarni A., Narayan R., 2013, *Astron. Astrophys.*, 559, A116
 Prakash M., Bombaci I., Prakash M., Ellis P. J., Lattimer J. M., Knorren R., 1997, *Physics Reports*, 280, 1
 Qian L., Abramowicz M. A., Fragile P. C., Horák J., Machida M., Straub O., 2009, *A&A*, 498, 471
 Radice D., Perego A., Hotokezaka K., Fromm S. A., Bernuzzi S., Roberts L. F., 2018, *ApJ*, 869, 130
 Rezzolla L., Zanotti O., 2013, *Relativistic Hydrodynamics*. Oxford University Press, Oxford
 Rezzolla L., Baiotti L., Giacomazzo B., Link D., Font J. A., 2010, *Classical and Quantum Gravity*, 27, 114105
 Shibata M., 2007, *Phys. Rev. D*, 76, 064035
 Stergioulas N., Friedman J. L., 1995, *ApJ*, 444, 306
 Uryū K., Tsokaros A., Baiotti L., Galeazzi F., Taniguchi K., Yoshida S., 2017, *Phys. Rev. D*, 96, 103011
 Varga R. S., 2000, *Matrix iterative analysis*, 2., rev. and expanded ed. No. 27 in Springer series in computational mathematics, Springer, Berlin Heidelberg
 Virtanen P., et al., 2020, *Nature Methods*, 17, 261
 Wessel E., Paschalidis V., Tsokaros A., Ruiz M., Shapiro S. L., 2021, *Phys. Rev. D*, 103, 043013
 Wielgus M., Fragile P. C., Wang Z., Wilson J., 2015, *MNRAS*, 447, 3593
 Will C. M., 1974, *ApJ*, 191, 521
 Witzany V., Jefremov P., 2018, *Astron. Astrophys.*, 614, A75

APPENDIX A: DETAILED CODE COMPARISON RESULTS

In Table A1, we list normalized values of the rest mass $\bar{M}_0 \equiv K^{-1/2(\Gamma-1)} M_0$ and the total angular momentum $\bar{J} \equiv K^{-1/(\Gamma-1)} J$ computed with our code for a set of rotating neutron star models used in [Nozawa et al. \(1998\)](#). All models were computed with the grid resolution $(N_s, N_\mu) = (401, 201)$. Neutron star parameters $(\rho_0^{\max}, r_p/r_e)$ corresponding to each model can be looked up from [Nozawa et al. \(1998\)](#).

This paper has been typeset from a $\text{\TeX}/\text{\LaTeX}$ file prepared by the author.